

Control and Learning in Biological Systems

A Dissertation Presented

by

Mahdiar Sadeghi

to

The Department of Electrical and Computer Engineering

in partial fulfillment of the requirements
for the degree of

Doctor of Philosophy

in

Electrical Engineering

Northeastern University
Boston, Massachusetts

July 2022

*To my father, Dr. Mohammad Sadeghi,
who taught me love, trust, and commitment.*

Contents

List of Figures	iv
List of Tables	v
List of Acronyms	vi
Acknowledgments	viii
Abstract of the Dissertation	ix
1 Background	1
1.1 Theory and practice	2
1.1.1 Gravitational waves	2
1.1.2 Genetic heredity	4
1.2 Focus of the dissertation	4
1.3 Organization of this work	5
2 Periodic Flow of Ribosomes	6
2.1 Introduction	6
2.1.1 Example	9
2.1.2 Periodic excitation	9
2.1.3 Bottleneck entrance	10
2.1.4 Problem Formulation	13
2.1.5 Structure of this chapter	13
2.2 Numerical simulations	13
2.2.1 Example	14
2.2.2 Harmonic functions	15
2.3 Optimal periodic control	16
2.3.1 The case $n = 1$	17
2.3.2 Pontryagin's maximum principle for periodic trajectories	18
2.3.3 The structure of an optimal control	20
2.4 A single stage RFM with two inputs	24
2.4.1 Pontryagin's maximum principle	25
2.4.2 Characterization of of regular arcs	26

2.4.3	Characterization of of singular arcs	26
2.4.4	Admissible Switching Patterns	28
2.4.5	Suboptimality of admissible switching patterns	32
2.5	Conclusion	33
3	Bispecific T-cell engagers	35
3.1	Introduction	35
3.2	Three-body model and the importance of binding kinetics	40
3.3	Identifiability	42
3.4	Optimal binding kinetics	45
3.5	Comparison between Bispecific T Cell Engagers (BiTE) antibodies	46
3.6	Bio-distribution	52
4	Epidemics	57
4.1	Optimal timing	58
4.2	Singular purterbation approach	59
A	First Appendix Headline	74
B	Second Appendix Headline	75

List of Figures

1.1	Theory and practice	3
2.1	Ribosome flow model	7
2.2	Cascade system	11
2.3	Traffic system illustration	12
2.4	Periodic gain in Example 2.2.1 as a function of ω	15
2.5	Numerical simulations	16
3.1	Three-body model	37
3.2	Steady state simulations	42
3.3	Bell-shape characteristics	47
3.4	Characteristics heatmap	48
3.5	Comparison of bell-shapes	50
3.6	Comparison of the characteristics of the bell-shapes	51

List of Tables

3.1	BiTE molecules	38
3.2	Parameters used in model (3.12).	54
3.3	Variables used in model (3.12).	55

List of Acronyms

AUC Area Under the Curve. The definite integral of a curve that describes the variation of a drug concentration in blood plasma as a function of time.

BiTE Bispecific T Cell Engagers. A type of fusion protein that is designed to harness the power of the immune system to treat cancer. These bispecific molecules are created by linking the targeting regions of two antibodies.

IV Intravenous Existing or taking place within, or administered into, a vein or veins

KIH Knob Into Holes A well-validated heterodimerization technology for the third constant domain of an antibody.

LIGO Laser Interferometer Gravitational-Wave Observatory. The definite integral of a curve that describes the variation of a drug concentration in blood plasma as a function of time.

LTi Linear Time-Invariant Is a system property that produces an output signal from any input signal subject to the constraints of linearity and time-invariance.

FDA Food and Drug Administration. The United States Food and Drug Administration is a federal agency of the Department of Health and Human Services.

MDOR Mathematically Derived Optimal Regimen.

MFI Maximum Fluorescence Intensity. Indicates the maximum light (photons) emitted. Fluorescence is created by the absorption of energy (light) by fluorescent molecules, called fluorophores.

MTD Maximum Tolerated Dose. The maximum tolerated dose is commonly estimated to be the maximum dose that can be administered for the duration of a specific study that will not compromise the survival of the animals by causes other than carcinogenicity.

NPI Nonpharmaceutical Intervention. Actions, apart from getting vaccinated and taking medicine, that people and communities can take to help slow the spread of illnesses like pandemic influenza (flu).

ODE Ordinary Differential Equation. In mathematics, an ordinary differential equation is a differential equation containing one or more functions of one independent variable and the derivatives of those functions.

- PMP** Pontryagin Maximum Principle. Is used in optimal control theory to find the best possible control for taking a dynamical system from one state to another, especially in the presence of constraints for the state or input controls.
- QSS** Quasi Steady State. A situation that is changing slowly enough that it can be considered to be constant.
- RFM** Ribosome Flow Model. A predictive model for the fundamental features of the translation process, including translation rates, protein abundance levels, ribosomal densities and the relation between all these variables.
- SCID** Severe combined immunodeficiency. SCID mice have a genetic immune deficiency that affects their B and T cells. Due to the lack of mature B and T lymphocytes, these mouse models are ideal for xenoengraftment of human cells and tissue.
- SISO** Single-Input Single-Output. In control theory, a single-input and single-output system is a simple single variable control system with one input and one output.
- SD** Social Distancing. In public health, social distancing, also called physical distancing, is a set of non-pharmaceutical interventions or measures intended to prevent the spread of a contagious disease by maintaining a physical distance between people and reducing the number of times people come into close contact with each other.
- TASEP** Totally asymmetric Simple Exclusion Process. Is a paradigm model in nonequilibrium statistical mechanics. It is a lattice model in which particles hop into a one-dimensional lattice from the left with rate α , jump along the lattice to the right with rate β and exit from the right with rate γ .
- TDB** T-cell-Dependent Bispecific. Similar to BiTE. A promising cancer immunotherapy that recruit a patient's T cells to kill cancer cells.
- TME** Tumor Micro-Environment. The ecosystem that surrounds a tumor inside the body.

Acknowledgments

Most of all, I would like to thank my dissertation advisor, Eduardo Sontag, a talented mathematician and passionate scientist. I am proud to say my experience with him was intellectually exciting and fun, and has energized me to continue in research. I sincerely hope I continue to have opportunities to interact with Eduardo for the rest of my research career.

I am indebted to Mario Sznajder who first showed me how magic happens with control theory. I would also like to thank the members of my dissertation committee - not only for their time and extreme patience, but for their intellectual contributions to my professional development. To Carey Rappaport, who was my master thesis advisor and first taught me how to use simple mathematical models to solve complicated problems. Without the appreciation and excitement in mathematical modeling inspired by him, I may not have ever pursued research in applied mathematics. To Prof. Bahram Shafaei, I thank for being a supportive, strong guiding force as Chair of my committee. To Irina Kareva, who helped train me to work on mathematical problems relevant to pharmaceutical industry. My experience working with Irina on chemotherapy and immunotherapy applications was extremely positive. To Mark Niedre, for having me at his lab in Fall 2015. Mark was the first person that I worked with in graduate school and I am grateful for his professional guidance.

To my groupmates, thanks for the fun and support. My experience in research was greatly enhanced as it filled out from M Ali, Tianchi, Phong, Shu, Zheming, Alon, and William. I look forward to having all of you as colleagues in the years ahead.

Abstract of the Dissertation

Control and Learning in Biological Systems

by

Mahdiar Sadeghi

Doctor of Philosophy in Communication, Control, and Signal Processing

Northeastern University, July 2022

Prof. Eduardo D. Sontag, Advisor

Theory and practice are the two fundamental tools in engineering and scientific research. With a great increase of quantitative experiments in biological systems over the past decades, mathematical modeling is able to enhance predictions and generate new hypotheses. A “good” model of a system, that is expected to reproduce the experimental observations, is capable of making predictions outside the previous experimental settings. However, the accuracy of predictions based on mathematical models highly depends on the assumptions used to model the system. The objective of this study is to explore possible approaches to deploy such models in order to find new hypotheses to be tested in future experimental settings. From the lens of control and decision-making, a few biological systems relevant to chemotherapy, immunotherapy, and epidemics are considered in this work. Models are analyzed numerically and analytically in order to enhance the outcome of the system with a new control/decision. A new dosing plan for chemotherapy is identified and evaluated via in-silico experiments to optimally reduce the tumor volume at the end of the plan. The new dosing plan consists of two doses starting with a small dose at the beginning of the plan and an increased dose after a few weeks. Unlike traditional chemotherapy plans currently used, the proposed plan is neither a maximum tolerated dose, nor a metronomic/intermittent plan. Moreover, epidemic models under social distancing guidelines are studied. Considering a single interval social distancing based on the start time and the duration of the social distancing shows a linear relationship between optimal timing of the social distancing. Models analyzed in this work are generic and applicable to wide a range of applications.

Chapter 1

Background

The goal of scientific research is to advance knowledge that does not exist in the literature. Research process starts with a specific question and proposing a hypothesis to answer it. Hypotheses are formed to come up with a solution to an unmet need, or in order to have a better understanding of a phenomena. The next step is testing the proposed hypothesis, which can be done in two ways. Finding an available data set based on previous experiments which can be used to evaluate the newly generated hypothesis, or designing a new experiment that can generate sufficient data for evaluating the hypothesis.

An in depth understanding of the scientific subject is necessary to come up with a new hypothesis or a new experiment design. Models are usefull in providing a simpler representation of a realworld phenomena, to have a better understanding and easy to test envonriment for creativity. In architecture, models are physical or computational 3D representation of a proposed building design to increase the construction speed and make the planning easier. In computing, emulators are hardware or software models the enable one computer to acts like another system. In biology, animal models are frequently used to create a realistic environment for biological experiments such as, immune cell and tumor, pharmacokinetics of a drug, or disease progression. In dynamic systems, mathematical models can be defined with Ordinary Differential Equation (ODE) to represent a mechanistic representation of the system. Mathematical models can be also defined in numerical formats such as, agent based models, and artificial neural networks. The creation of scientific fields like theoretical biology, math biology, systems biology, computational biology, or systems and computational medicine are all based on using mathematical models in theoretical studies of biological systems. These studeis are interdisciplinary and require collaboration of people with different backgrounds. A simple analogy is that, understanding biology requires chemistry, understanding chemistry requires physics, and

CHAPTER 1. BACKGROUND

understanding physics requires math.

The objective is to perform numerical and analytical analysis from the control theory perspective. The techniques used in control theory, which deals with the control of dynamical systems in engineered processes and machines, can be applied to mathematical models of biological systems. Medicine can be thought as a control input for a biological system like an animal or a human. Also, considering the spread of an epidemic disease in a society as a biological system, Nonpharmaceutical Intervention (NPI) like social distancing can be thought as a control input. The following section is about the role of mathematical modeling in theory and practice. A couple of well-known examples are discussed to illustrate the importance of modeling in scientific research. The focus and organisation of this study is discussed at the end of this chapter.

1.1 Theory and practice

Theory and practice are the two fundamental tools in scientific research. Classic biology has been thought as a practical science. With a great increase of quantitative experiments in biological systems over the past decades, more theoretical studies are possible in biology.

Figure 2.5a presents a visual representation of the connection between theory and practice. In theory, models that are based on the existing knowledge (data) are being used in order to come up with new hypotheses. Some of the newly generated hypothesis can be tested by using the existing data, which is common in data science. Other hypotheses require a new data set being generated for testing. In practice a hypothesis that is formed based on the existing knowledge, have to be tested with a new experiment design. In the following, two of the most important scientific discoveries as an example of the presented analogy between theory and practice.

1.1.1 Gravitational waves

By considering models as a framework to generalize the previous experimental data. One could have the power of predicting the results of experiments that has not existed before. The discovery of gravitational waves is one the most important examples for models that could predict above and beyond the present data.

Gravity has been the most basic and mysterious force in physics. Understanding gravity is one of the examples that started with theory and mathematical models. Einstein predicted gravitational waves in 1937 [1] based on his theory of relativity. But the universe's gravitational

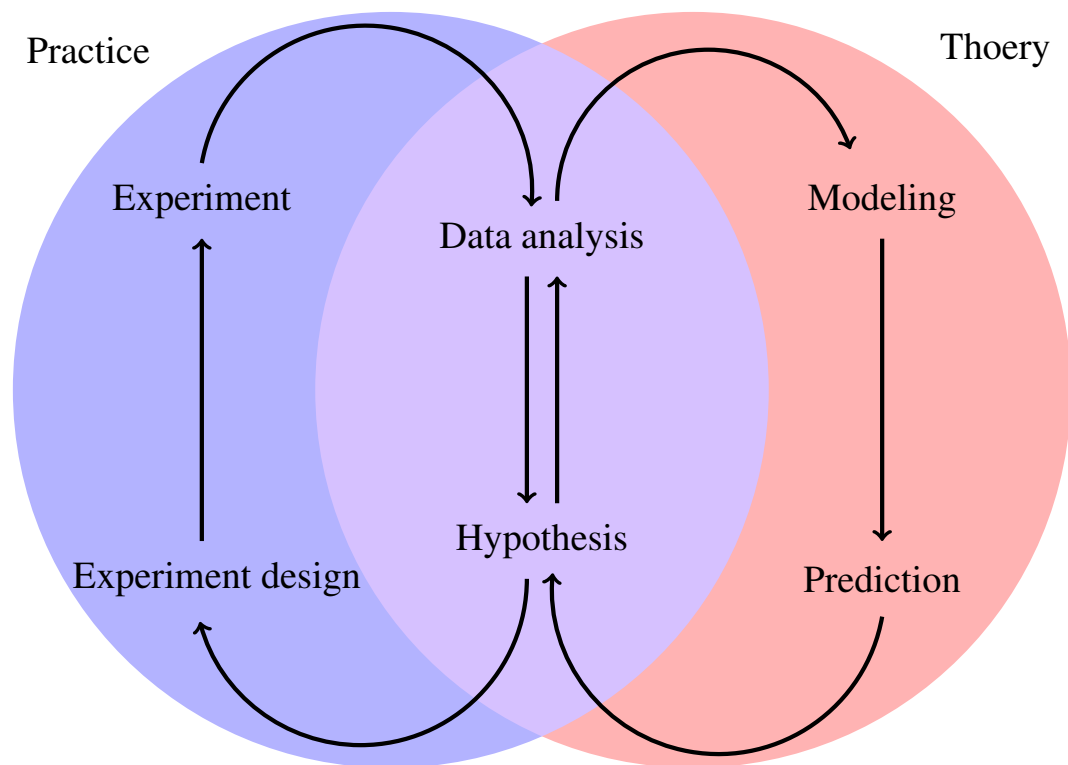


Figure 1.1: Theory and practice in research: In practice, the left circle, the objective is to come up with a new experiment design that can produce a data set for answering a scientific hypothesis. In theory, the right circle, the objective is to use a model that *reasonably* represents the existing data to come up with new predictions and hypotheses. In data science, the objective is to come up with new hypotheses that can be answered with the existing data sets, which is becoming more popular.

CHAPTER 1. BACKGROUND

waves have not been detected until 2015, when a large group of researchers used Laser Interferometer Gravitational-Wave Observatory (LIGO), and they recieved the 2017 Nobel prise in physics.

1.1.2 Genetic heredity

A scientific descovery without a proper model is missing a key feature. Genetic heredity is one of the most imporant examples for this scenario. Hypothesis could be frequently made from the data, but whether the hypothesis is true or not requires regorious analysis. Statistical analysis, that are based on statistical models, are frequently used in data science to answer hypothetical questions from the data.

Mendel used pea plants for cross-breeding experiments to discover the fundamental laws of genetic inheritance [2]. The discovery of the law of segregation, the law of indepdents assortment, and the law of dominance took him eight years, when he grew over 10,000 pea plants to track their genetic heredity. Mendel's dicoverly was not widely accepted in scientific communities until Fisher pushlished a statistical analysis of Mendel's data [3].

1.2 Focus of the dissertation

Trial and error has been the fundamental method in practice. Trial comes from the Anglo-French trier meaning “to try”, and error means “a mistake”. The procedue of trial and error strats by testing a hypothesis that might pass or fail, and iterating over modified versions of the starting hypothesis until it gets to a desired solution. The focus of this work is to utalize mathematical models in order to speed up the trail and error process. The number of possible experiment designs are often at a combinatorial scale, and mathematical models are necessary to bring more insight into the problem to optimize the number of tries.

Most achievements of biotechnology in pharmaceutical industry on *platform* thinking. *platform* is a machine that could automatically repeat exeriments with the desired inputs. *Platforms* are automated systems that enable scientist to make new discoveries with more depth, and speed. In other words, if the left hand side of Figure 2.5a (practice) is automated then scientist could spend more time on biology, the right hand side of Figure 2.5a (theory), to deepen their understanding to make new discoveries. The focus of this dissertation is the theoretical aspect of biological discoveries. For example, performing feasability study to answer hypothetical questions of the experimentalists, or optimization study to identify what changes of the input could optimize the objective.

1.3 Organization of this work

Each of the following chapter in this work consists of using mathematical models for control of a biological systems. The contributions made in this work are both mathematical and computational based on the very specific applications. Each chapter is written independently. While, the models used here are considered to be generic and applicable to applications outside the focus of each study. The reader is encouraged to consider specific chapters of their interest.

Chapter 2 is based on a dynamic model of translation process, Ribosome Flow Model (RFM). This project started by a question from one of the experimentalist, who thought it could be possible to change the inflow/outflow rates of ribosomes experimentally, and asked if the mRNA translation speed can be increased by using a periodic input. Early numerical results of the model was not in favor of periodic inputs. Meanwhile, theoretically it became an interesting task to prove that constant inputs are always better for such a system. The rest of this dissertation is less theoretical. Chapter 4 discusses social distancing in compartmental epidemic models. Chapter 3 is dedicated to bispecific T-cell engagers.

Chapter 2

Periodic Flow of Ribosomes

This chapter is based on a compartmental model for ribosome flow during RNA translation called the Ribosome Flow Model (RFM). This model includes a set of positive transition rates that control the flow from every site to the consecutive site. It has been shown that when these rates are time-varying and jointly T -periodic every solution of the RFM converges to a unique periodic solution with period T . In other words, the RFM entrains to the periodic excitation. In particular, the protein production rate converges to a unique T -periodic pattern. From a biological point of view, one may argue that the average of the periodic production rate, and not the instantaneous rate, is the relevant quantity. The problem that this chapter investigates can be roughly stated as: can periodic rates yield a higher average production rate than constant rates in RFM? This question is rigorously formulated and shown via simulations, and rigorous analysis in one simple case, that the answer is no.

2.1 Introduction

Transcription and translation are the two major steps of gene expression, that is, the transformation of the information encoded in the DNA into proteins. During translation complex molecular machines called ribosomes traverse the mRNA molecule, “read” it codon by codon, and generate the corresponding chain of amino-acids [4].

New imaging techniques [5–8] and empirical approaches [9–14] for studying gene expression provide unprecedented amounts of data on the dynamics of translation. This increases the need for mathematical and computational models for ribosome flow that can integrate, explain and make predictions based on this data (see the reviews [15–17]). Mechanistic models are particularly

CHAPTER 2. PERIODIC FLOW OF RIBOSOMES

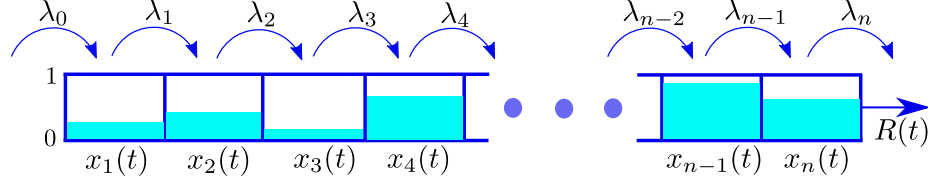


Figure 2.1: A visual representation for Ribosome Flow Model (RFM).

important in biotechnology and synthetic biology, as they allow to predict the effect of various manipulations of the biological machinery [18, 19].

The RFM is a deterministic model for ribosome flow [20]. It can be derived via a dynamic mean-field approximation of a fundamental model from statistical physics called the Totally asymmetric Simple Exclusion Process (TASEP) [15, 21]. In TASEP particles hop randomly along a chain of ordered sites. A site can be either free or contain a single particle. Totally asymmetric means that the flow is unidirectional, and simple exclusion means that a particle can only hop into a free site. This models the fact that two particles cannot be in the same place at the same time. Note that this generates an indirect coupling between the particles. In particular, if a particle is delayed at a site for a long time then the particles behind it cannot move forward and thus a “traffic jam” may evolve.

The RFM is a compartmental model with n sites. The state-variable $x_i(t)$, $i = 1, \dots, n$, describes the density of particles at site i at time t . This is normalized so that $x_i(t) = 0$ [$x_i(t) = 1$] means that site i is completely empty [full] at time t . The state-space is thus the closed unit cube $[0, 1]^n$.

The dynamics is described by n first-order ODEs:

$$\dot{x}_1(t) = \lambda_0(1 - x_1(t)) - \lambda_1 x_1(t)(1 - x_2(t)), \quad (2.1a)$$

$$\dot{x}_k(t) = \lambda_{k-1} x_{k-1}(t)(1 - x_k(t)) - \lambda_k x_k(t)(1 - x_{k+1}(t)), \quad 2 \leq k \leq n-1, \quad (2.1b)$$

$$\dot{x}_n(t) = \lambda_{n-1} x_{n-1}(t)(1 - x_n(t)) - \lambda_n x_n(t). \quad (2.1c)$$

Here $\lambda_i > 0$ is a parameter that describes the transition rate from site i to site $i + 1$, with λ_0 [λ_n] called the entry [exit] rate. Eq. (2.1) can be explained as follows. The flow from site k to site $k + 1$ is given by $\lambda_k x_k(1 - x_{k+1})$, i.e. it increases when site k becomes fuller and decreases when site $k + 1$ becomes fuller. This is a “soft” version of simple exclusion. The production rate at time t is the rate of ribosomes exiting site n , that is, $R(t) := \lambda_n x_n(t)$. Figure 2.1 is a visual representation of RFM.

In the context of mRNA translation, the λ_i ’s depend on various biomechanical properties for example the abundance of tRNA molecules that deliver the amino-acids to the ribosomes. A

CHAPTER 2. PERIODIC FLOW OF RIBOSOMES

recent paper suggests that cells vary their tRNA abundance in order to control the translation rate [22].

Note that if λ_k is small for some k then the flow from site k to site $k + 1$ will be small, so site k fills up, that is $x_k(t)$ will be close to one for all t sufficiently large. Consequently, the flow $\lambda_{k-1}x_{k-1}(1 - x_k)$ from site $k - 1$ to site k will become small and then site $k - 1$ fills up. In this way, a traffic jam may evolve behind a “bottleneck” site. The implications of such traffic jams in various biological transport processes is recently attracting considerable interest (see, e.g. [23, 24]).

It has been shown [25] that there exists a unique $e = e(\lambda_0, \dots, \lambda_n) \in (0, 1)^n$ such that any solution of the RFM emanating from the unit cube converges to e . Thus, the system is globally asymptotically stable. In particular, the production rate converges to the steady-state value

$$R := \lambda_n e_n. \quad (2.2)$$

Ref. [26] derived a spectral representation for the steady-state density e and production rate R . Given the RFM, define the $(n + 2) \times (n + 2)$ tridiagonal matrix:

$$B := \begin{bmatrix} 0 & \lambda_0^{-1/2} & 0 & 0 & \dots & 0 & 0 \\ \lambda_0^{-1/2} & 0 & \lambda_1^{-1/2} & 0 & \dots & 0 & 0 \\ 0 & \lambda_1^{-1/2} & 0 & \lambda_2^{-1/2} & \dots & 0 & 0 \\ & & & \vdots & & & \\ 0 & 0 & 0 & \dots & \lambda_{n-1}^{-1/2} & 0 & \lambda_n^{-1/2} \\ 0 & 0 & 0 & \dots & 0 & \lambda_n^{-1/2} & 0 \end{bmatrix}. \quad (2.3)$$

Note that B is (componentwise) nonnegative and irreducible. Let $\sigma > 0$ [$\zeta \in \mathbb{R}_{>0}^{n+2}$] denote the Perron root [Perron vector] of B (see e.g. [27]). Then

$$R = \sigma^{-2} \text{ and } e_i = \frac{\zeta_{i+2}}{\lambda_i^{1/2} \sigma \zeta_{i+1}}, \quad i = 1, \dots, n. \quad (2.4)$$

In other words, the steady-state values can be determined without any numerical simulations of the dynamics but rather using (efficient and numerically stable) algorithms for determining the Perron root and vector of tridiagonal matrices. Note that it follows from (2.4) that

$$R(c\lambda_0, \dots, c\lambda_n) = cR(\lambda_0, \dots, \lambda_n), \quad \text{for all } c > 0, \quad (2.5)$$

that is, the steady-state production rate is positively homogeneous of degree one.

CHAPTER 2. PERIODIC FLOW OF RIBOSOMES

2.1.1 Example

Consider the RFM with all the rates equal to one. Then B is a tridiagonal Toeplitz matrix and it is well-known (see e.g. [28]) that its eigenvalues are

$$2 \cos\left(\frac{k\pi}{n+3}\right), \quad k = 1, \dots, n+2, \quad (2.6)$$

so the Perron root is $\sigma = 2 \cos\left(\frac{\pi}{n+3}\right)$. The corresponding Perron vector is

$$\zeta = \left[\sin\left(\frac{\pi}{n+3}\right) \quad \sin\left(\frac{2\pi}{n+3}\right) \quad \dots \quad \sin\left(\frac{(n+2)\pi}{n+3}\right) \right]^T. \quad (2.7)$$

Thus, in this case (2.4) gives

$$R = \frac{1}{4} \left(\cos\left(\frac{\pi}{n+3}\right) \right)^{-2} \quad (2.8)$$

and

$$e_i = \frac{\zeta_{i+2}}{\sigma \zeta_{i+1}} \quad (2.9a)$$

$$= \frac{\sin\left(\frac{(i+2)\pi}{n+3}\right)}{2 \cos\left(\frac{\pi}{n+3}\right) \sin\left(\frac{(i+1)\pi}{n+3}\right)} \quad (2.9b)$$

for all $i = 1, \dots, n$. For example, in the one-dimensional case, i.e. $\dot{x}_1 = 1 - 2x_1$ it is clear that the equilibrium point is $e = 1/2$, so $R = 1/2$, whereas (2.8) yields

$$R = \frac{1}{4} \left(\cos\left(\frac{\pi}{4}\right) \right)^{-2} = 1/2, \quad (2.10)$$

and (2.9a) gives

$$e_1 = \frac{\sin\left(\frac{3\pi}{4}\right)}{2 \cos\left(\frac{\pi}{4}\right) \sin\left(\frac{2\pi}{4}\right)} = 1/2. \quad (2.11)$$

2.1.2 Periodic excitation

Biological organisms are exposed to periodic excitations like the 24h solar day and the periodic cell-cycle division process. Proper functioning often requires entrainment to such excitations i.e. internal processes must operate in a periodic pattern with the same period as the excitation. An example is the sleep-wake cycle that entrains to the 24h day.

Ref. [29] studied the RFM with positive time-varying rates that are jointly T -periodic, and proved that every state-variable $x_i(t)$ converges to a periodic solution with period T . In other words, the RFM entrains. The proof is based on the fact that the RFM is an (almost) contractive system [30,

CHAPTER 2. PERIODIC FLOW OF RIBOSOMES

31]. However, this provides no information on the attractive periodic solution (except for its period). Obtaining such information is a difficult problem (see [32] and the references therein).

Since any set of jointly periodic rates induces a periodic solution, a natural question is: can periodic rates yield a higher production rate than constant rates? In this paper, we formulate this question rigorously, and show that it can be cast as an optimal control problem.

2.1.3 Bottleneck entrance

In an analogous point of view, the RFM can be thought as a “bottleneck entrance”. And generalized to more applications like traffic systems, and scheduling at security checks with a cascade of an arbitrary Hurwitz positive linear system. The cascade system entrains i.e. in response to a T -periodic inflow every solution converges to a unique T -periodic solution of the system. And, the objective would be to choose a periodic inflow rate with a given mean value that maximizes the average outflow rate of the system when maximizing the throughput is crucial.

The occupancy at time t in such applications can be modeled by the normalized state-variable $x(t) \in [0, 1]$. In traffic systems, $x(t)$ can be interpreted as the number of vehicles relative to the maximum capacity of a highway segment. For the security check, it is the number of passengers at a security gate relative to its capacity. In biological transport models discussed in the previous sections, $x(t)$ is interpreted as the probability that a biological “machine” (e.g. ribosome, motor protein) is bound to a specific segment of the “trail” it is traversing (e.g. mRNA molecule, filament) at time t .

The output in such systems is a nonnegative outflow which can be interpreted as the rate of cars exiting the highway for the traffic system, or passengers leaving the gate for the security check. The inflow rates are often periodic, such as those controlled by traffic light signals, or periodic flight schedules. Proper functioning often requires *entrainment* to such excitations i.e. internal processes must operate in a periodic pattern with the same period as the excitation [33]. In this case, in response to a T -periodic inflow the outflow converges to a T -periodic pattern, and the *throughput* is then defined as the ratio of the average outflow relative to the average inflow over the period T .

As a general model for studying such applications is the cascade of two systems shown in Fig. 2.2. The first block is called the *bottleneck* and is given by:

$$\dot{x}(t) = \sigma(t)(1 - x(t)) - \lambda x(t), \quad (2.12a)$$

$$w(t) = \lambda x(t), \quad (2.12b)$$

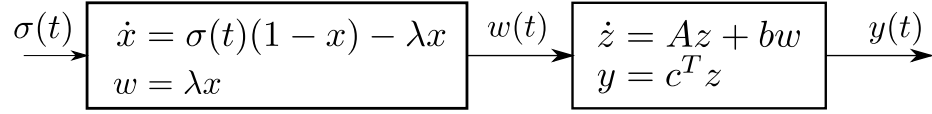


Figure 2.2: Cascade system: the bottleneck is feeding a positive linear system.

where $\sigma(t) > 0$ is the inflow rate at time t , $x(t) \in [0, 1]$ is the occupancy of the bottleneck, and $\lambda > 0$ controls the output flow $w(t)$. The rate of change of the occupancy is proportional to the inflow rate $\sigma(t)$ and the *vacancy* $1 - x(t)$, that is, as the occupancy increases the effective entry rate decreases.

A standard notation in this study. Vectors [matrices] are denoted by small [capital] letters. For a vector x , x' denotes the transpose of x . To follow the standard practice of identifying any two measurable functions that are identical except perhaps on a set of measure zero.

Assuming that the inflow is periodic with period $T \geq 0$, i.e. $\sigma(t + T) = \sigma(t)$ for all $t \geq 0$. The occupancy $x(t)$ (and thus also $w(t)$) entrains, as the system is contractive [34, 35]. In other words, for any initial condition $x(0) \in [0, 1]$ the solution $x(t)$ converges to a unique T -periodic solution denoted x_σ and thus w converges to a T -periodic solution w_σ .

The outflow of the bottleneck is the input into a Hurwitz positive linear system:

$$\dot{z} = Az + bw, \quad (2.13a)$$

$$y = c^T z, \quad (2.13b)$$

where $A \in \mathbb{R}^{n \times n}$ is Hurwitz and Metzler and $b, c \in \mathbb{R}_+^n$ (see Figure 2.2). It is clear that for a T -periodic $\sigma(t)$, all trajectories of the cascade converge to a unique trajectory $(x_\sigma(t), z_\sigma(t))$ with $x_\sigma(t) = x_\sigma(t + T)$ and $z_\sigma(t) = z_\sigma(t + T)$.

The objective for these applications is to compare the average (over a period) of $y_\sigma(t)$ for various T -periodic inflows. To make a meaningful comparison, consider inflows that have a fixed mean $\bar{\sigma} > 0$, i.e

$$\frac{1}{T} \int_0^T \sigma(t) dt = \bar{\sigma}. \quad (2.14)$$

The objective is maximize the gain of the system from σ to y , i.e to maximize $\int_0^T y_\sigma(t) dt$ for inputs with mean $\bar{\sigma}$.

The trivial periodic inflow rate is the constant rate $\sigma(t) \equiv \bar{\sigma}$. To compare the outflow for this constant inflow with that obtained for an inflow that switches between two values σ_1 and σ_2 such that $\sigma_2 > \bar{\sigma} > \sigma_1 > 0$. In other words, $\sigma(t) \in \{\sigma_1, \sigma_2\}$ is periodic and satisfies (2.14).

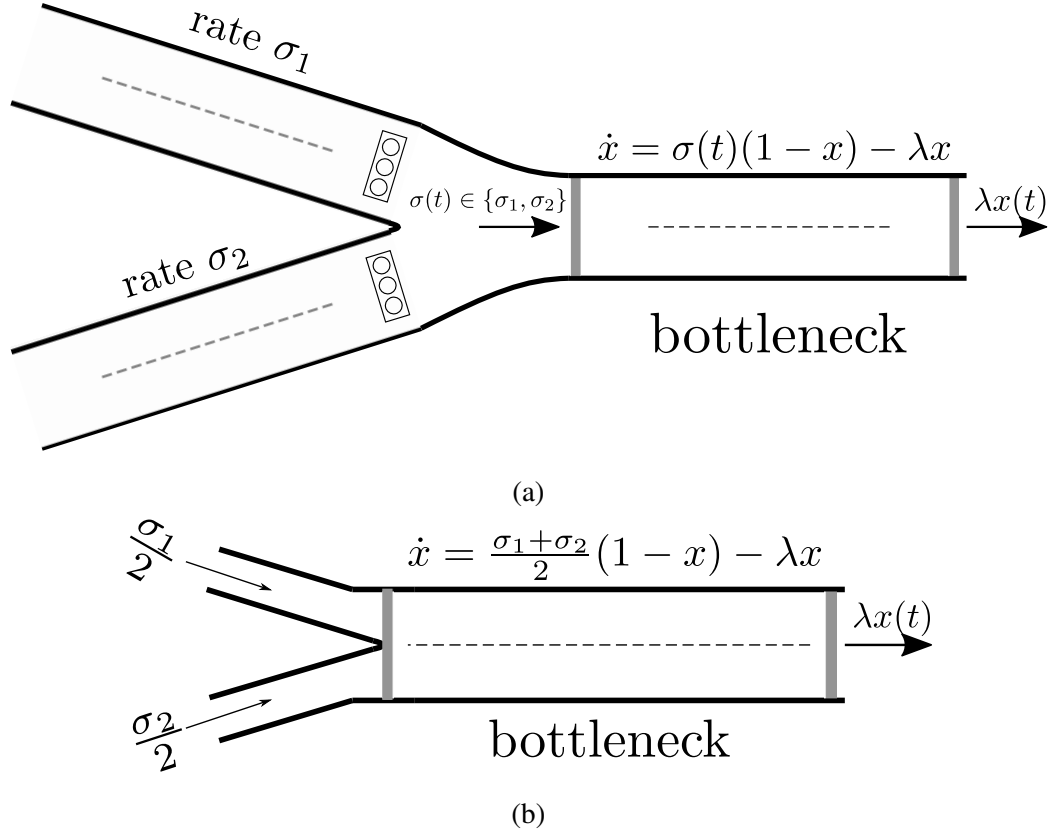


Figure 2.3: Traffic system application illustrating the two strategies. Here $x(t) \in [0, 1]$ denotes the occupancy of the bottleneck at time t . (a) The inflow rate switches via periodically-varying traffic lights between two flows with rates σ_1, σ_2 . At each time, either vehicles in the upper lane or vehicles in the lower lane can enter the bottleneck, but not both. (b) The double lane of each flow is restricted to a single lane and connected directly to the corresponding lane in the bottleneck.

For the application in traffic system depicted in Figure 2.3, there are two flows of vehicles with different rates σ_1, σ_2 (e.g., cars and trucks) each moving in a separate road and joining into a two-lane highway. This can be done in two ways. The first is to place traffic lights at the end of each road, and switch between them before entering the highway as in Figure 2.3(a). The periodic traffic light signal $\sigma(t)$ switches between the two flows, hence $\sigma(t) \in \{\sigma_1, \sigma_2\}$. The second strategy is to have each road constricted to a single lane, and then each joining the corresponding lane in the highway as in Figure 2.3(b). Hence, the inflow rate is constant and equal to $(\sigma_1 + \sigma_2)/2$. In both cases, the occupancy $x(t)$ of the highway is modeled by (2.12a). For a proper comparison, $\frac{1}{T} \int_0^T \sigma(t) dt = (\sigma_1 + \sigma_2)/2$ as discussed before.

2.1.4 Problem Formulation

For any T -periodic function f , with $T > 0$, let $\bar{f} := \frac{1}{T} \int_0^T f(t) dt$, that is, the average of f over a period. Pick a set of rates $\lambda_i(t)$, $i = 1, \dots, n$, that are jointly T -periodic (note that a constant rate is T -periodic for any T). This induces a unique T -periodic trajectory $\gamma(t)$ of the RFM and thus a unique T -periodic production rate $R_T(t) := \lambda_n(t)\gamma_n(t)$ [29]. The average production rate is thus \bar{R}_T . Consider an RFM with constant rates $\bar{\lambda}_i$, $i = 1, \dots, n$. Recall that every trajectory converges to a unique steady-state e and thus to a production rate $R := \bar{\lambda}_n e_n$.

The question of interest in this study is: what is the relation between \bar{R}_T and R ? Note that this is a “fair” comparison as we replace every time-varying rate by its average value.

More generally, we can take a set of admissible rates $S_{a,T}$ that are all jointly T -periodic and satisfy $\bar{\lambda}_i = a_i$. Recall $\sup_{S_{a,T}} \{\bar{R}_T/R\}$, where the sup is with respect to all the (non-trivial) rates in $S_{a,T}$, the *periodic gain* of the RFM over $S_{a,T}$. One can argue that the average production rate over a period, rather than the instantaneous value, is the biologically relevant quantity. Then a periodic gain larger than one implies that we can “do better” using periodic rates. A periodic gain one implies that we do not “lose” anything with respect to the constant rates $\lambda_i(t) \equiv a_i$. A periodic gain smaller than one implies that for any (non-trivial) periodic rate the average production rate is lower than the one obtained for constant rates. This implies that entrainment always incurs a cost, as the production rate for constant rates is higher.

2.1.5 Structure of this chapter

The remainder of this paper is organized as follows. Section 2.2 describes some simulation results for the general RFM. Section 2.3 shows that the problem of finding the periodic gain can be cast as an optimal control problem. This implies that the problem can be addressed using known and powerful tools from optimal control theory [36–38]. By applying Pontryagin Maximum Principle (PMP) to analyze a particular case, namely, a one-dimensional RFM with a constant λ_1 and a time-varying and periodic $\lambda_0(t)$.

2.2 Numerical simulations

To gain a wider perspective, consider the case of a Single-Input Single-Output (SISO) asymptotically stable Linear Time-Invariant (LTI) system with input [output] $u(t)$ [$y(t)$] and transfer

CHAPTER 2. PERIODIC FLOW OF RIBOSOMES

function $G(s)$. Fix $\omega, a > 0$. Suppose that the set of admissible inputs is

$$\{a + b \sin(\omega t) : b \in \mathbb{R}\}.$$

Note that every input here is T -periodic with $T := 2\pi/\omega$, and that $\bar{u} = a$. It is well-known that for $u(t) = a + b \sin(\omega t)$ the output converges to the T -periodic function $y_T(t) := |G(0)|a + |G(j\omega)|b \sin(\omega t + \angle G(j\omega))$, where $j := \sqrt{-1}$, so $\bar{y}_T = |G(0)|a$. On the other-hand, if we replace $u(t)$ by a constant input with value $\bar{u} = a$ then the output converges to $|G(0)|a$. Thus, the periodic gain for this set of admissible inputs is one and by superposition it is one for any set of admissible T -periodic inputs with average a .

Of course, for nonlinear systems, like the RFM, the periodic gain may be different than one. The next example demonstrates this.

2.2.1 Example

Consider the scalar system

$$\dot{x}(t) = 1 - x(t)u(t). \quad (2.15)$$

For

$$u(t) = 1 + (1/2) \cos(\omega t), \quad (2.16)$$

with $\omega > 0$, the solution is

$$x(t) = \exp\left(-t - \frac{\sin(\omega t)}{2\omega}\right)(x(0) + \phi(t)), \quad (2.17)$$

where $\phi(t) := \int_0^t \exp\left(s + \frac{\sin(\omega s)}{2\omega}\right) ds$. In particular, for $T := 2\pi/\omega$,

$$x(T) = \exp(-T)(x(0) + \phi(T)). \quad (2.18)$$

Now determine an initial condition $x(0) = c$ for which the solution is T -periodic, that is,

$$c = \exp(-T)(c + \phi(T)), \quad (2.19)$$

so

$$c = \frac{\exp(-T)\phi(T)}{1 - \exp(-T)}. \quad (2.20)$$

Thus, the periodic solution is $x_T(t) := \exp\left(-t - \frac{\sin(\omega t)}{2\omega}\right)(c + \phi(t))$. It is not difficult to show that this solution is attractive.

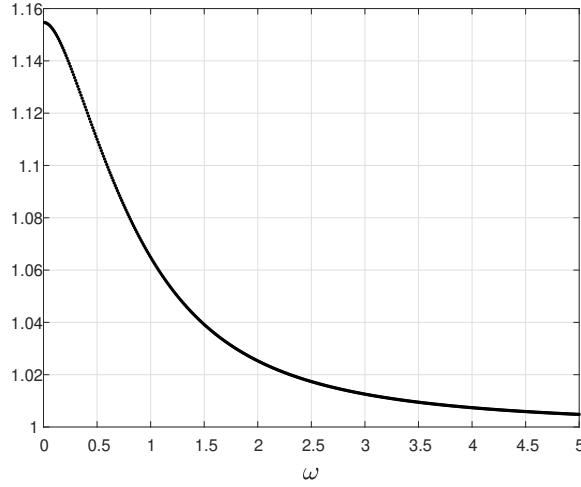


Figure 2.4: Periodic gain in Example 2.2.1 as a function of ω .

On the other-hand, for a constant control with value $\bar{u} = \frac{1}{T} \int_0^T u(s) \, ds = 1$, the solution of (2.15) converges to the steady-state 1 and thus the periodic gain for the control (2.16) is $\bar{x}_T = \frac{1}{T} \int_0^T x_T(t) \, dt$. Fig. 2.4 depicts \bar{x}_T as a function of ω . It may be seen that the periodic gain is always larger than 1, and that it approaches 1 as $\omega \rightarrow \infty$.

2.2.2 Harmonic functions

The RFM where every rate is a sum of m harmonic functions with random coefficients. More precisely, we generated a matrix of random entries $P \in \mathbb{R}^{(n+1) \times (2m)}$ and then set

$$\lambda_i(t) = 1 + \sum_{k=1}^m (p_{i,2k-1} \sin(k\omega t) + p_{i,2k} \cos(k\omega t)), \quad i = 0, \dots, n. \quad (2.21)$$

Note that this guarantees that the λ_i 's are jointly T -periodic for $T = 2\pi/\omega$ and that $\bar{\lambda}_i = 1$ for all i . The entries of P are generated randomly with a uniform distribution over $[-1/(2m), 1/(2m)]$, so that $\lambda_i(t) \geq 0$ for all i and all t .

The RFM with $n = 1$ is simulated first. Since $\bar{\lambda}_i = 1$ for $i = 0, 1$, and example 2.2.1, it can be concluded that $R = 1/2$. Fig. 2.5a depicts a histogram of the average steady-state flow \bar{R}_T for $m = 3$ and 10,000 random simulations. It may be seen that \bar{R}_T is always smaller than $1/2$. Thus, the constant rates yield the maximal production rate.

To explain this, consider the case where $\lambda_1 = 1$ and $\lambda_0(t) = 1 + \sin(\omega t)$. Let us compare this to the case where $\lambda_1 = 1$ and $\lambda_0 = 1$. At times t such that $\sin(\omega t) = -1$, there is less flow

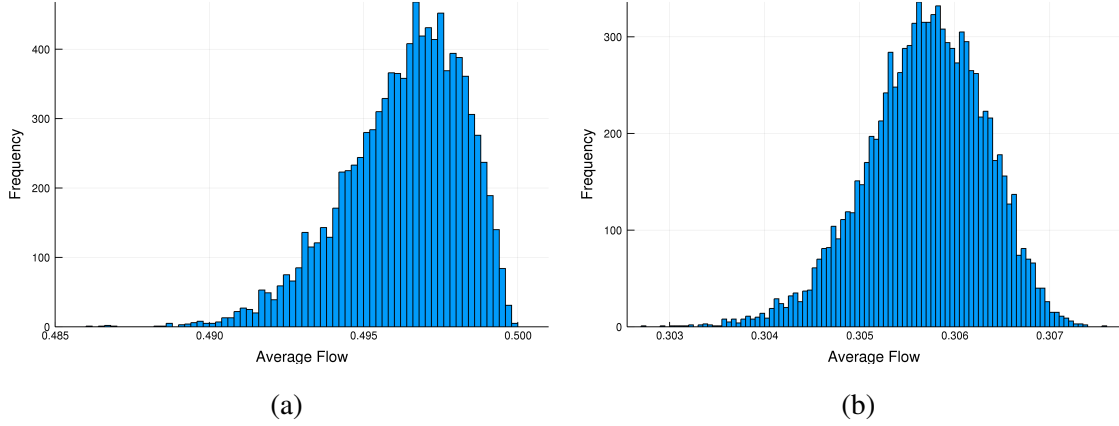


Figure 2.5: Numerical simulations: (a) A histogram of $\overline{R_T}$ values in the one-dimensional RFM with random periodic $\lambda_0(t)$ and $\lambda_1(t)$. (b) A histogram of $\overline{R_T}$ values in an RFM with $n = 4$ and periodic rates $\lambda_i(t)$, $i = 0, \dots, 4$.

because $\lambda_0(t) = 0$. At times t such that $\sin(\omega t) = 1$, there is more flow because $\lambda_0(t) = 2$, but then λ_1 becomes a bottleneck rate and slows down the flow, and thus on average we don't gain enough flow to compensate for what is lost. This might be called the “casino effect”: on average, the gains are not enough to compensate for the losses.

Consider now an RFM with $n = 4$ and constant rates set to one. By (2.8),

$$R = \frac{1}{4}(\cos(\pi/7))^{-2} \approx 0.307979. \quad (2.22)$$

Fig. 2.5b depicts a histogram representation of $\overline{R_T}$ calculated over 10,000 simulations of an RFM with random periodic rates $\lambda_0(t), \dots, \lambda_4(t)$. It may be seen that $\overline{R_T}$ is smaller than the value in (2.22), so again the constant rates are those that maximize the production rate.

2.3 Optimal periodic control

The next goal is to pose the problem of determining the RFM periodic gain as an optimal control problem. The equations of the RFM can be augmented with an additional state-variable as

CHAPTER 2. PERIODIC FLOW OF RIBOSOMES

follows

$$\dot{z}_1 = \lambda_0(1 - z_1) - \lambda_1 z_1(1 - z_2), \quad (2.23a)$$

$$\dot{z}_k = \lambda_{k-1} z_{k-1}(1 - z_k) - \lambda_k z_k(1 - z_{k+1}), \quad 2 \leq k \leq n-1, \quad (2.23b)$$

$$\dot{z}_n = \lambda_{n-1} z_{n-1}(1 - z_n) - \lambda_n z_n, \quad (2.23c)$$

$$\dot{z}_{n+1} = \lambda_n z_n, \quad z_{n+1}(0) = 0. \quad (2.23d)$$

Thus, $z(t) = \int_0^t R(\tau) d\tau$. Pick $T > 0$ and $a_1, \dots, a_n > 0$, and let $S_{a,T}$ denote the set of measurable functions $\lambda_i : [0, T] \rightarrow \mathbb{R}_+$ such that $\overline{\lambda_i} = a_i, i = 0, \dots, n$.

By applying the spectral representation to determine the steady-state production rate R when $\lambda_i(t) \equiv a_i$ for all i . Thus, determining the periodic gain is equivalent to solving the following optimization problem.

Problem 1. Maximize $\frac{1}{T} z_{n+1}(T)$ over the set of admissible rates $S_{a,T}$ with the boundary condition $z_i(0) = z_i(T) \in (0, 1)$ for $i = 1, \dots, n$.

The last condition guarantees that we are maximizing the production rate along the (unique) periodic trajectory. This optimal control problem can be addressed using known tools from optimal control theory [36–38]. This special case can be demonstrated as follows.

2.3.1 The case $n = 1$

Pick $T, a_0 > 0$, and consider the problem of computing the periodic gain of the one-dimensional RFM with a constant $\lambda_1 > 0$ and a time-varying $\lambda_0 : [0, T] \rightarrow \mathbb{R}_+$ with $\overline{\lambda_0} = a_0$.

Consider first the special case where $\lambda_0(t)$ is constant. Then clearly $\lambda_0(t) \equiv a_0$, and thus

$$\dot{x}_1 = a_0(1 - x_1) - \lambda_1 x_1. \quad (2.24)$$

The steady-state of this equation is $e_1 = \frac{a_0}{a_0 + \lambda_1}$, so $\overline{R} = \frac{\lambda_1 a_0}{a_0 + \lambda_1}$.

To study the case where $\lambda_0(t)$ is not constant, it is useful to incorporate the constraint $\overline{\lambda_0} = a_0$ into the dynamics. Thus, the following system is considered.

$$\dot{x}_1(t) = \lambda_0(t)(1 - x_1(t)) - \lambda_1 x_1(t), \quad (2.25a)$$

$$\dot{x}_2(t) = \lambda_0(t), \quad (2.25b)$$

with the boundary conditions

$$x_1(T) = x_1(0), \quad x_2(0) = 0, \quad x_2(T) = T a_0. \quad (2.26)$$

Fix $L \geq 2a_0$. Determining the periodic gain is equivalent to solving the following problem.

CHAPTER 2. PERIODIC FLOW OF RIBOSOMES

Problem 2. Find $\lambda_0 : [0, T] \rightarrow [0, L]$ that maximizes the cost functional

$$J := \frac{1}{T} \int_0^T \lambda_1 x_1(t) dt, \quad (2.27)$$

subject to the dynamics (2.25) and the boundary conditions (2.26).

The added bound on the size of $\lambda_0(t)$ is needed because the presented solution in this study is using the PMP.

Note that the model (2.25) can be rewritten as a bilinear control system.

$$\dot{x} = f(x) + g(x)u, \quad (2.28)$$

where u represents λ_0 , $f(x) := \begin{bmatrix} -\lambda_1 x_1 & 0 \end{bmatrix}'$, and $g(x) := \begin{bmatrix} 1 - x_1 & 1 \end{bmatrix}'$. Thus, Problem 2 is a nonlinear optimal control problem (for other control problems for the RFM, see [39]).

The main result of this study can be stated as:

Theorem 1. For any $L \geq 2a_0$ the unique solution of Problem 2 is the constant rate:

$$\lambda_0^*(t) \equiv a_0, \quad (2.29)$$

and the corresponding optimal cost is:

$$J^* = \frac{\lambda_1 a_0}{\lambda_1 + a_0}. \quad (2.30)$$

Hence, the steady-state average flow of the system cannot be improved by using a periodic rate.

The proof of Theorem 1 is based on applying the PMP to analyze the structure of optimal controls.

2.3.2 Pontryagin's maximum principle for periodic trajectories

We apply the PMP to Problem 2. The statement of the PMP in our case is standard, except perhaps for the constraint that forces maximization over the periodic solution, i.e. $x_1(0) = x_1(T)$.

Define the Hamiltonian

$$\mathcal{H}(u, x, p, p_0) := p' (f(x) + g(x)u) + \frac{1}{T} p_0 \lambda_1 x_1 \quad (2.31a)$$

$$= (-p_1 \lambda_1 + p_0 \frac{1}{T} \lambda_1) x_1 + (p_1 (1 - x_1) + p_2) u, \quad (2.31b)$$

where $p(t) := \begin{bmatrix} p_1(t) & p_2(t) \end{bmatrix}'$ is the adjoint, and $p_0 \geq 0$ is called the abnormal multiplier. Note that we can scale the Hamiltonian by scaling u and λ_1 . Thus, from here on we assume without loss of generality that $\lambda_1 = 1$.

CHAPTER 2. PERIODIC FLOW OF RIBOSOMES

Proposition 2 (PMP). *Let $u^*(t) : [0, T] \rightarrow [0, L]$ be an optimal control for Problem 2. Let $x^* : [0, T] \rightarrow ([0, 1] \times \mathbb{R}_+)$ be the corresponding optimal trajectory. Let $p_0^* := T$. There exists a function $p^* : [0, T] \rightarrow \mathbb{R}^2 \setminus \{0\}$ such that:*

1. *The functions $x^*(t)$ and $p^*(t)$ satisfy:*

$$\dot{x}^* = \frac{\partial \mathcal{H}}{\partial p}(u^*, x^*, p^*, p_0^*), \quad (2.32a)$$

$$\dot{p}^* = -\frac{\partial \mathcal{H}}{\partial x}(u^*, x^*, p^*, p_0^*); \quad (2.32b)$$

2. *The control $u^*(t)$ satisfies*

$$\mathcal{H}(s, x^*(t), p^*(t), p_0^*) \leq \mathcal{H}(u^*(t), x^*(t), p^*(t), p_0^*) \quad (2.33)$$

for all $s \in [0, L]$ and almost every (a.e.) $t \in [0, T]$;

3. *The adjoint satisfies the transversality condition:*

$$p_1^*(0) = p_1^*(T). \quad (2.34)$$

A few remarks will be discussed before proving Proposition 2. First, note that (2.32a) yields

$$\dot{p}_1^* = (1 + u)p_1^* - 1, \quad \dot{p}_2^* = 0. \quad (2.35)$$

so $p_2^*(t) \equiv p_2^*(0)$. Second, define the *switching function* $\varphi^* : [0, T] \rightarrow \mathbb{R}$ by

$$\varphi^*(t) := (p^*(t))'g(x^*(t)) \quad (2.36a)$$

$$= p_1^*(t)(1 - x_1^*(t)) + p_2^*(0). \quad (2.36b)$$

Note that $\varphi^*(t)$ is absolutely continuous. Then (2.33) implies that

$$u^*(t) = \begin{cases} L, & \varphi^*(t) > 0, \\ 0, & \varphi^*(t) < 0. \end{cases} \quad (2.37)$$

A calculation yields

$$\dot{\varphi}^* = \dot{p}_1^*(1 - x_1^*) - p_1^*\dot{x}_1^* \quad (2.38a)$$

$$= p_1^* - 1 + x_1^*, \quad (2.38b)$$

$$\ddot{\varphi}^* = \dot{p}_1^* + \dot{x}_1^* \quad (2.38c)$$

$$= (1 - x_1^* + p_1^*)u - 1 - x_1^* + p_1^*. \quad (2.38d)$$

Note that this implies that $\dot{\varphi}^*$ is absolutely continuous, so $\varphi^* \in C^1$.

CHAPTER 2. PERIODIC FLOW OF RIBOSOMES

Proof of Proposition 2. Most of the statements here are the standard PMP. It is only necessary to prove the transversality condition (2.34), and that $p_0^* \neq 0$.

Pick $S \subseteq \mathbb{R}^4$, and suppose that the state must satisfy the constraint $\begin{bmatrix} x(0) & x(T) \end{bmatrix}' \in S$. Then the transversality condition [37] is

$$\begin{bmatrix} p(0) \\ -p(T) \end{bmatrix} \perp_{\mathcal{T}} \begin{bmatrix} x(0) \\ x(T) \end{bmatrix} S, \quad (2.39)$$

where $\mathcal{T}_z S$ is the tangent space of S at z . In this case, $S = \{z \in \mathbb{R}^4 \mid z_1 - z_3 = 0, z_2 = 0, z_4 = Ta_0\}$. Hence, $\mathcal{T}_z S = \text{span}\{[1, 0, 1, 0]'\}$. Therefore, it is necessary that $p_1^*(0) = p_1^*(T)$.

Next we show that the abnormal multiplier is not zero. Assume that $p_0^* = 0$. Then (2.32a) yields

$$p_1^* = (1 + u^*)p_1^*. \quad (2.40)$$

Thus, $p_1^*(t) \geq \exp(t)p_1^*(0)$ for all $t \geq 0$. If $p_1^*(0) \neq 0$ then this contradicts (2.34), so we conclude that $p_1^*(0) = 0$ and thus $p_1^*(t) \equiv 0$. This implies that $p_2^*(0) \neq 0$, and thus (2.36a) and (2.37) imply that $u^*(t)$ is constant. But in this case it is clear that $u^*(t) \equiv a_0$. It can be concluded that by assuming $p_0^* \neq 0$, and by scaling the result is $p_0^* = T$. \square

2.3.3 The structure of an optimal control

Given an optimal control u^* , let

$$E_+^* := \{t \in [0, T] : \varphi^*(t) > 0\}, \quad (2.41a)$$

$$E_-^* := \{t \in [0, T] : \varphi^*(t) < 0\}, \quad (2.41b)$$

$$E_0^* := \{t \in [0, T] : \varphi^*(t) = 0\}. \quad (2.41c)$$

Note that all these sets are measurable.

The next result analyzes singular arcs. For a measurable set $F \subseteq [0, T]$, we use $\mu(F)$ to denote the Lebesgue measure of F .

Lemma 3. *Suppose that u^* is an optimal control such that $\mu(E_0^*) > 0$. Then there exists a unique $c_0 \in (0, L]$ such that*

$$u^*(t) \equiv c_0 \text{ for a.e. } t \in E_0^*, \quad (2.42)$$

and

$$x_1^*(t) \equiv \frac{c_0}{1 + c_0} \text{ for all } t \in E_0^*. \quad (2.43)$$

CHAPTER 2. PERIODIC FLOW OF RIBOSOMES

Proof. Let $E^* \subseteq E_0^*$ denote the set of accumulation points of E_0^* . Note that $\mu(E^*) = \mu(E_0^*)$, since $E_0^* - E^*$ is the set of isolated points of E^* which is countable, and hence has measure zero. For $t \in E^*$, we have $\varphi^*(t) = 0$, so $(\varphi^*(t))^{(k)} := \frac{d^k}{dt^k} \varphi^*(t) = 0$ for any integer $k \geq 0$.

The equation $\varphi^*(t) = \dot{\varphi}^*(t) = 0$ yields $p_1^*(t)(1 - x_1^*(t)) \equiv -p_2^*(0)$, and $p_1^*(t) \equiv 1 - x_1^*(t)$.

It can be concluded that

$$p_1^*(t) \equiv 1 - x_1^*(t) \equiv r, \quad (2.44)$$

where r is a constant. Since $x^*(t) \in (0, 1)$, $r \in (0, 1)$. Hence, $p_2^*(0) = -r^2 < 0$.

Combining (2.44) with the fact that $\ddot{\varphi}^*(t) = 0$ yields

$$u^*(t) \equiv c_0, \quad (2.45)$$

where $c_0 := \frac{1-r}{r}$. Note that since $u^*(t) \leq L$,

$$r(1 + L) \geq 1. \quad (2.46)$$

Now (2.44) yields $x_1^*(t) \equiv 1 - r = \frac{c_0}{1+c_0}$. \square

Note that if $r(1 + L) = 1$ then on any singular arc we have $u^*(t) = c_0 = L$. This case is “not interesting” as then we can identify the singular arc with a bang arc. Thus from here on the assumption is that

$$r(1 + L) > 1. \quad (2.47)$$

The notation $B[S]$ is used to denote a bang [singular] arc. The bang arc can be either B_+ (i.e. $\varphi^*(t) > 0$ on the arc), or B_- . The next result considers the concatenation of singular and bang arcs.

Proposition 4. *An optimal control u^* cannot contain a concatenation of arcs in the form SBS.*

Proof. Suppose that u^* includes a concatenation SBS. It is already known that there exists a unique value r such that $x_1^*(t) \equiv 1 - r$ and $p_1^*(t) \equiv r$ on both singular arcs.

Suppose that $B = B_-$. Then $\dot{x}_1^* = -x_1^*$ along the bang arc, so $x_1^*(t)$ strictly decreases on B_- . But this is a contradiction, as $x_1^*(t)$ must have the same value on both singular arcs.

Suppose now that $B = B_+$. Then

$$\dot{p}_1^* = (1 + L)p_1^* - 1^* \quad (2.48)$$

along the bang arc. In particular, at the initial time $\tau \in (0, T)$ of B_+ ,

$$\dot{p}_1^*(\tau) = (1 + L)r - 1^* \quad (2.49)$$

CHAPTER 2. PERIODIC FLOW OF RIBOSOMES

and (2.47) yields $\dot{p}_1^*(\tau) > 0$. Combining this with (2.48) implies that $p_1^*(t)$ strictly increases on B_+ and this is again a contradiction. \square

The next result analyzes optimal controls that include two consecutive bang arcs.

Lemma 5. *An optimal control u^* cannot include any of the following concatenations: $B_-B_+B_-$, B_-B_+S , $B_+B_-B_+$, and B_+B_-S .*

Proof. Suppose that u^* includes B_+B_- . Then there exists $\tau \in (0, T)$ such that $\varphi^*(t) > 0$ for $t \in (\tau - \varepsilon, \tau)$, and $\varphi^*(t) < 0$ for $t \in (\tau, \tau + \varepsilon)$, with $\varepsilon > 0$. Hence $\varphi^*(\tau) = 0$ and $\dot{\varphi}^*(\tau) \leq 0$. Combining this with (2.38a) yields

$$p_1^*(\tau) - 1 + x_1^*(\tau) \leq 0. \quad (2.50)$$

For any $t \in (\tau, \tau + \varepsilon)$ it is true that $u^*(t) = 0$, so $\dot{x}_1^*(t) = -x_1^*(t)$ and $\dot{p}_1^*(t) = p_1^*(t) - 1$. Thus,

$$x_1^*(t) = \exp(-(t - \tau))x_1^*(\tau), \quad (2.51a)$$

$$p_1^*(t) = 1 + \exp(t - \tau)(p_1^*(\tau) - 1). \quad (2.51b)$$

Substituting this in (2.38a) yields

$$\dot{\varphi}^*(t) = \exp(t - \tau)(p_1^*(\tau) - 1) + \exp(-(t - \tau))x_1^*(\tau) \quad (2.52a)$$

$$< \exp(t - \tau)(p_1^*(\tau) - 1 + x_1^*(\tau)), \quad (2.52b)$$

where the last equation follows from the fact that along the periodic solution $x_1^*(s) \in (0, 1)$ for all s . Combining this with (2.50) implies that

$$\dot{\varphi}^*(t) < 0 \text{ for all } t \in (\tau, \tau + \varepsilon). \quad (2.53)$$

This clearly implies that $\varphi^*(t) < 0$ for all $t \in (\tau, T]$. Thus, the concatenations B_+B_-S and $B_+B_-B_+$ are not possible. A similar argument shows that if u^* includes B_-B_+ then the concatenations B_-B_+S and $B_-B_+B_-$ are not possible. \square

The analysis above implies that the most general form possible for an optimal control is

$$B_1SB_2B_3, \quad (2.54)$$

where every B_i stands for either B_- or B_+ . Our next goal is to compare a control u with such a structure to the control that includes a single singular arc. To do this, it is necessary to explicitly compute and compare the cost J along such controls. The following lemma is used in the solution of a scalar switched system.

CHAPTER 2. PERIODIC FLOW OF RIBOSOMES

Lemma 6. *Pick $b_1 > b_2 > 0$ and $a_1, a_2 \in \mathbb{R}$. Suppose that starting from $y(0) = y_0$ and follow the dynamics $\dot{y} = a_1 - b_1 y$ for $t \in [0, t_1]$, with $t_1 > 0$, and then switch to $\dot{y} = a_2 - b_2 y$ for $t \in [t_1, t_1 + t_2]$, with $t_2 > 0$, and such that $y(t_1 + t_2) = y_0$ (that is, the system returns to its initial state). Then*

$$\int_0^{t_1+t_2} y(t) dt < t_1 c_1 + t_2 c_2 + \frac{t_1 t_2 (b_1 - b_2)(c_1 - c_2)}{b_1 t_1 + b_2 t_2}, \quad (2.55)$$

where $c_i := a_i / b_i$.

Proof. First consider the scalar equation $\dot{y} = a - by$, with $b \neq 0$, $y(t_0) = y_0$ and $y(t_1) = y_1$. Then integration yields

$$y_1 - y_0 = \int_{t_0}^{t_1} (a - by(t)) dt = a(t_1 - t_0) - b \int_{t_0}^{t_1} y(t) dt, \quad (2.56)$$

so

$$\int_{t_0}^{t_1} y(t) dt = (t_1 - t_0) \frac{a}{b} - \frac{y_1 - y_0}{b}. \quad (2.57)$$

Now fix $b_1 > b_2 > 0$. Suppose that starting from $y(0) = y_0$ we follow the dynamics $\dot{y} = a_1 - b_1 y$ for $t \in [0, t_1]$, with $t_1 > 0$, and then switch to $\dot{y} = a_2 - b_2 y$ for $t \in [t_1, t_1 + t_2]$, with $t_2 > 0$, such that $y(t_1 + t_2) = y_0$. That is, the system returns to its initial state. Then

$$y(t_1) = c_1(1 - \exp(-b_1 t_1)) + \exp(-b_1 t_1) y_0, \quad (2.58a)$$

$$y(t_1 + t_2) = c_2(1 - \exp(-b_2 t_2)) + \exp(-b_2 t_2) y(t_1), \quad (2.58b)$$

where $c_i := a_i / b_i$. Denoting $y_1 := y(t_1)$ and using the fact that $y(t_1 + t_2) = y_0$ yields

$$y_1 = c_1(1 - \exp(-b_1 t_1)) + \exp(-b_1 t_1) (c_2(1 - \exp(-b_2 t_2)) + \exp(-b_2 t_2) y_1), \quad (2.59a)$$

$$y_0 = c_2(1 - \exp(-b_2 t_2)) + \exp(-b_2 t_2) (c_1(1 - \exp(-b_1 t_1)) + \exp(-b_1 t_1) y_0), \quad (2.59b)$$

so

$$y_1 - y_0 = (c_1 - c_2) \frac{(1 - \exp(-b_1 t_1))(1 - \exp(-b_2 t_2))}{1 - \exp(-b_1 t_1 - b_2 t_2)}. \quad (2.60)$$

It is straightforward to show that for any $v, w > 0$ we have

$$\frac{(1 - \exp(-v))(1 - \exp(-w))}{1 - \exp(-(v + w))} < \frac{vw}{v + w}, \quad (2.61)$$

so we obtain the bound

$$y_1 - y_0 < (c_1 - c_2) \frac{b_1 b_2 t_1 t_2}{b_1 t_1 + b_2 t_2}. \quad (2.62)$$

CHAPTER 2. PERIODIC FLOW OF RIBOSOMES

On the other-hand, (2.57) yields

$$\int_0^{t_1+t_2} y(t) dt = \int_0^{t_1} y(t) dt + \int_{t_1}^{t_1+t_2} y(t) dt \quad (2.63a)$$

$$= t_1 c_1 - \frac{y_1 - y_0}{b_1} + t_2 c_2 - \frac{y_0 - y_1}{b_2} \quad (2.63b)$$

$$= t_1 c_1 + t_2 c_2 + (y_1 - y_0)(b_2^{-1} - b_1^{-1}). \quad (2.63c)$$

Using (2.62) and the fact that $b_1 > b_2 > 0$ yields (2.55) and this completes the proof. \square \square

The next result completes the proof of Theorem 1.

Lemma 7. *If u^* has the form (2.54) then u^* includes a single singular arc.*

2.4 A single stage RFM with two inputs

Consider the scalar system with two inputs over a compact time interval $[0, T]$:

$$\dot{x} = u_0(t)(1 - x(t)) - u_1(t)x(t),$$

with the integral constraints $\int_0^T u_0(t)dt = T\bar{u}_0$, $\int_0^T u_1(t)dt = T\bar{u}_1$. The one-dimensional problem with integral constraints can be lifted to a three dimensional system with boundary conditions as follows:

$$\dot{x}_1(t) = u_0(t)(1 - x_1(t)) - u_1(t)x_1(t), \quad (2.64a)$$

$$\dot{x}_2(t) = u_0(t), \quad (2.64b)$$

$$\dot{x}_3(t) = u_1(t). \quad (2.64c)$$

with the boundary conditions

$$x_1(T) = x_1(0), \quad x_2(0) = 0, \quad x_2(T) = T\bar{u}_0, \quad x_3(0) = 0, \quad x_3(T) = T\bar{u}_1. \quad (2.65)$$

Given two positive numbers ℓ, L with $\ell < L$, the optimal control problem can be stated as follows:

Problem 3. *Find $u_0, u_1 : [0, T] \rightarrow [\ell, L]$ that maximizes the cost functional*

$$J := \frac{1}{T} \int_0^T u_1(t)x_1(t) dt, \quad (2.66)$$

subject to the dynamics (2.64a) and the boundary conditions (2.65).

CHAPTER 2. PERIODIC FLOW OF RIBOSOMES

The result can be stated as follows:

Theorem 8. *For any ℓ, L with $0 < \ell \leq \bar{u}_0/(\bar{u}_1 + \bar{u}_0) \leq L$, the optimal cost for Problem 3 is*

$$J^* = \frac{\bar{u}_0}{\bar{u}_1 + \bar{u}_0}. \quad (2.67)$$

and it can be achieved by the following inputs:

$$u_0^*(t) \equiv \bar{u}_0, u_1^*(t) \equiv \bar{u}_1. \quad (2.68)$$

Remark 1. *The control inputs that achieve the optimal cost are not unique, since if the two control inputs are coupled via the equation $u_0(t)/\bar{u}_0 \equiv u_1(t)/\bar{u}_1$ then system will be given by:*

$$\dot{x}_1(t) = u_0(t) \left(1 - \frac{\bar{u}_1 + \bar{u}_0}{\bar{u}_0} x_1(t) \right).$$

Then any measurable function u_0 will achieve J^ given in (2.67).*

2.4.1 Pontryagin's maximum principle

Consider Problem 8, let the $p(t) = [p_1(t), p_2(t), p_3(t)]$ be the accompanying co-state vector. The associated Hamiltonian can be written as:

$$\mathcal{H} = (p_1(t)(1 - x_1(t)) + p_2(t))u_0(t) + (x_1(t)(1 - p_1(t)) + p_3(t))u_1(t). \quad (2.69)$$

The time-evolution of the co-state is given by the following ODE:

$$\dot{p} = \begin{bmatrix} (u_0(t) + u_1(t))p_1(t) - u_1(t) \\ 0 \\ 0 \end{bmatrix}, \quad (2.70)$$

with the boundary condition $p_1(0) = p_1(1)$.

Hence, two of the co-states are constants and are given by

$$p_2(t) \equiv p_2(0), p_3(t) \equiv p_3(0). \quad (2.71)$$

In what follows, let $\mathcal{X} := (u_0^*(t), u_1^*(t), x^*(t), p^*(t))$ be an optimal trajectory. We first state the following lemma:

Lemma 9. *Let \mathcal{X} be an optimal trajectory. Then $x_1^*(t), p_1^*(t) \in (\frac{\ell}{L+\ell}, \frac{L}{\ell+L})$ for all $t \in [0, T]$.*

CHAPTER 2. PERIODIC FLOW OF RIBOSOMES

Proof. For the sake of contradiction, assume that $x(0) > L/(L + \ell)$. Since $u_0, u_1 \in [\ell, L]$, the comparison principle implies $\dot{x}(t) > 0$ for all t . Hence $x(T) > x(t)$, which contradicts $x(T) = x(0)$. The argument can be repeated if $x(0) < \ell/(L + \ell)$. Hence $x(0) = x(T) \in (\frac{\ell}{L+\ell}, \frac{L}{L+\ell})$. Now assume that $\exists t^* \in (0, T)$ such that $x(t^*) > L/L + \ell > x(T)$, the same argument shows that $x(t) > x(T)$ for all $t \in (t^*, T]$ which is a contradiction. The argument can be repeated if $x(t^*) < \ell/(L + \ell)$. A similar argument can be made to prove the corresponding statement for $p_1(t)$. \square

2.4.2 Characterization of regular arcs

There are two inputs, so there are two switching functions:

$$\varphi_0(t) = p_1(1 - x_1) + p_2(0) \quad (2.72a)$$

$$\varphi_1(t) = x_1(1 - p_1) + p_3(0). \quad (2.72b)$$

A regular arc is one in which the switching functions do not vanish when evaluated at it. Since the Hamiltonian is linear in the control input, then the optimal control is bang-bang when the switching function does not vanish. This is stated in the following Lemma:

Lemma 10. *Let \mathcal{X} be an optimal trajectory, then if $\varphi_i(t) \neq 0$, $i = 0, 1$ then:*

$$u_i^*(t) = \begin{cases} L & : \varphi_i(t) > 0 \\ \ell & : \varphi_i(t) < 0 \end{cases}, \quad (2.73)$$

i.e, $u_i(t)$ is a bang-bang control when corresponding switching function does not vanish.

Proof. Without loss of generality, let $i = 0$. Let $\varphi_0(t) > 0$, and let $u_0^*(t) < L$. However,

$$\mathcal{H}(u_0^*(t), u_1^*(t), x^*(t), p^*(t)) = \varphi_1(t)u_1^*(t) + \varphi_0(t)u_0^*(t) < \varphi_1(t)u_1^*(t) + \varphi_0(t)L = \mathcal{H}(L, u_1^*(t), x^*(t), p^*(t)), \quad (2.74)$$

which violates condition 3 in Proposition 2. Hence, $u_0^*(t) < L$ is not optimal. The same argument can be applied when $\varphi_0(t) < 0$, and also for $i = 1$. \square

2.4.3 Characterization of singular arcs

Given an optimal trajectory \mathcal{X} , let

$$E_+^i := \{t \in [0, T] : \varphi_i^*(t) > 0\}, \quad (2.75a)$$

$$E_-^i := \{t \in [0, T] : \varphi_i^*(t) < 0\}, \quad (2.75b)$$

$$E_0^i := \{t \in [0, T] : \varphi_i^*(t) = 0\}, \quad (2.75c)$$

CHAPTER 2. PERIODIC FLOW OF RIBOSOMES

where $i = 0, 1$. Note that all these sets are measurable.

We also need the time derivatives of the switching functions:

$$\dot{\varphi}_0(t) = u_1(t)(p_1 - (1 - x_1)) \quad (2.76a)$$

$$\dot{\varphi}_1(t) = u_0(t)(1 - x_1 - p_1). \quad (2.76b)$$

Note that $\dot{\varphi}_0, \dot{\varphi}_1$ are bounded, and continuous almost everywhere. Note also that the $\text{sgn}(\dot{\varphi}_0(t)) = -\text{sgn}(\dot{\varphi}_1(t))$, which will be used later.

In this subsection the interest is in the case with $\mu(E_0^i) > 0$ for either $i = 0$ or $i = 1$. A few lemmas are provided to characterize the system behaviour in such case.

Lemma 11. *Let \mathcal{X} be an optimal trajectory, and assume that $\mu(E_0^i) > 0$ for $i \in \{0, 1\}$. Then there exists $c_i \in (\frac{\ell}{L+\ell}, \frac{L}{\ell+L})$ such that*

$$x_1^*(t) \equiv c_i \text{ for all } t \in E_0^{i'}. \quad (2.77)$$

where $E_0^{i'}$ is the set of accumulation points of E_0^i . Furthermore, the two inputs must be satisfying the following relationship:

$$u_0(t) \equiv \frac{c_i}{1 - c_i} u_1(t), t \in E_0^{i'}. \quad (2.78)$$

Proof. Let $E_0^{i'} \subseteq E_0^i$ denote the set of accumulation points of E_0^i . Note that $\mu(E_0^{i'}) = \mu(E_0^i)$, since $E_0^i - E_0^{i'}$ is the set of isolated points of E_0^i which is countable, and hence has measure zero. For $t \in E_0^{i'}$, the $\varphi_i^*(t) = 0$, so $(\varphi^*(t))^{(k)} := \frac{d^k}{dt^k} \varphi^*(t) = 0$ for any integer $k \geq 0$.

W.l.o.g, let $i = 0$. The equation $\varphi_0^*(t) = \dot{\varphi}_0^*(t) = 0$ yields $p_1^*(t)(1 - x_1^*(t)) \equiv -p_2^*(0)$, and $p_1^*(t) \equiv 1 - x_1^*(t)$. In conclusion

$$p_1^*(t) \equiv 1 - x_1^*(t) \equiv 1 - c_0, \quad (2.79)$$

where c_0 is a constant. Since $x^*(t) \in (0, 1)$, $r \in (0, 1)$. Hence, $p_2^*(0) = -c_0^2 < 0$. The same argument can be repeated when $i = 1$.

Since $x_1(t)$ is constant, then $\dot{x}(t) \equiv 0$ and (2.78) follows. \square

The results above leave the possibility that $c_0 \neq c_1$. The following lemma provides further restrictions.

Lemma 12. *Let \mathcal{X} be an optimal trajectory. Then:*

1. *If $\mu(E_0^0 \cap E_0^1) > 0$, then $E_0^{0'} = E_0^{1'}$, and $\exists c \in (0, 1)$ such that $x(t) \equiv c$ when $t \in E_0^{0'}$.*

CHAPTER 2. PERIODIC FLOW OF RIBOSOMES

2. If $\mu(E_0^0 \cap E_0^1) = 0$, and $\mu(E_0^0) > 0$. Then $\dot{\varphi}_1(t) \equiv 0$ and there exists a constant $\bar{\varphi}_1 \neq 0$ such that $\varphi_1(t) = \bar{\varphi}_1 \neq 0$ on $t \in E_0^{0'}$. A parallel statement hold be exchanging $i = 0$ with $i = 1$.

Proof. The two statements can be proved as follows:

1. Let c_0, c_1 be given as in Lemma 11. Since $\mu(E_0^0 \cap E_0^1) > 0$, then $c_0 = c_1$, which also uniquely determines $p_2(0), p_3(0)$. Hence, $E_0^{0'} = E_0^{1'}$.
2. The assumptions imply that $\varphi_0^*(t) = \dot{\varphi}_0^*(t) \equiv 0$ for $t \in E_0^{0'}$. Using (2.76a),(2.76b), it can be written that $\dot{\varphi}_1(t) = 0$ if $\dot{\varphi}_0(t) = 0$. Since $x(t), p_1(t)$ on $E_0^{0'}$ are constant hence $\varphi_1(t) \equiv \bar{\varphi}_1 := c_0^2 + \lambda_3(0)$.

□

The last lemma shows that an optimal trajectory has two disjoint case for the singular arcs. Either each singular arc has both switching functions vanishing together, or only one of them can vanish at a time.

2.4.4 Admissible Switching Patterns

In the previous subsection we have shown that the optimal control can either be a bang-bang or singular. On the singular arc, the controls need to satisfy (2.78) but the state is constant, hence the value of the free input has no effect on the dynamics since $\dot{x}_1 = 0$ on all singular arcs. In general, there can be an arbitrary switching between these cases. In this part, the class of admissible switching patterns become more restricted.

Assuming that control inputs are *piecewise continuous*, and hence the switching functions are piecewise differentiable. An *arc* is the restriction of the optimal trajectory \mathcal{X} onto a maximal time interval such that the switching functions have a constant sign on that interval. Hence, the optimal trajectory \mathcal{X} can be decomposed into a sequences of arcs.

In order to facilitate the discussion we define the concept of an *arc sign* as an ordered pair. An arc has a sign $s = (s_0, s_1) \in \mathcal{S}^2 := \{0, +, -\}^2$ iff $\text{sgn}(\varphi_i(t)) \equiv s_i$ for $i = 0, 1$. Let s^j, s^k be the signs of two consecutive arcs. An *arc transition* is an ordered tuple of arc signs, and is represented as follows: $s^j \rightarrow s^k$. The *reverse* of an arc transition $s^j \rightarrow s^k$ is $s^k \rightarrow s^j$. A switching transition is said to be *inadmissible* if it can not occur in an optimal trajectory.

Some arc transitions are excluded in the following lemma:

CHAPTER 2. PERIODIC FLOW OF RIBOSOMES

Lemma 13. *Let \mathcal{X} be an optimal trajectory. Then the following arc transitions and their reverses are inadmissible: $(+, +) \rightarrow (-, -)$, $(0, 0) \rightarrow (+, +)$, $(0, 0) \rightarrow (-, -)$.*

Proof. Consider two consecutive arcs with a transition time τ . Hence, there exists $\varepsilon > 0$ such that the first arc defined on a time interval $(\tau - \varepsilon, \tau)$ with sign $(+, +)$, and second arc defined on $(\tau, \tau + \varepsilon)$ with sign $(-, -)$. Since both switching functions change sign from positive to negative at τ , then we have $D_\tau^+ \varphi_i(t) \leq 0, i = 0, 1$, where D_τ^+ is the upper right Dini's derivative at τ ¹. This also implies that $\exists \varepsilon_2 \leq \varepsilon$ such that $\dot{\varphi}_i(t) < 0$ for $t \in (\tau, \tau + \varepsilon_2), i = 0, 1$. But this contradicts (2.76a),(2.76b) which imply that $\text{sgn}(\dot{\varphi}_0(t)) = -\text{sgn}(\dot{\varphi}_1(t))$. So this means that transition $(+, +) \rightarrow (-, -)$ can not be realized by any trajectory, including an optimal trajectory \mathcal{X} .

A similar argument can be provided for all other cases. \square

Let (s_0, s_1) be the sign of an arc. An arc sign's entry s_i is said to be *locked* to $s \in \mathcal{S}$ if all subsequent arcs have signs with $s_i = s$. An arc sign's entry written as $\square s$ means that entry is locked to $s \in \mathcal{S}$. For example, an arc with the sign $(\square +, -)$ means that all subsequent arcs have a sign of the form $(+, s)$ for some $s \in \mathcal{S}$. The notation $(s_0, s_1) \rightarrow (\square s, s^*)$ means that the transition result in the first entry being locked to s . Similarly $(s_0, s_1) \rightarrow (s^*, \square s)$ means that the second entry will be locked to s .

The following lemma is based on the notation introduced above:

Lemma 14. *Let \mathcal{X} be an optimal trajectory, and consider two consecutive arcs. Then $\forall s \in \mathcal{S}$, a transition of the form $(+, s) \rightarrow (-, +)$ is equivalent to $(+, s) \rightarrow (\square, +)$. The parallel statements also hold with $(-, s) \rightarrow (\boxplus, -)$, $(s, +) \rightarrow (+, \square)$, $(s, -) \rightarrow (-, \boxplus)$.*

Proof. Consider the transition $(+, s) \rightarrow (-, +)$, and let τ be the transition time. Then, $\varphi_0(t) > 0$ on $(\tau - \varepsilon_2, \tau)$ and $\varphi_0(t) < 0$ on $(\tau, \tau + \varepsilon_1)$, where $\varepsilon_1, \varepsilon_2 > 0$ are the duration of each of the two arcs, respectively. By Lemma 10, we have $u_0(t) \equiv \ell, u_1(t) \equiv L$ for $t \in (\tau, \tau + \varepsilon_1)$. Similar to the proof of the previous lemma, $D_\tau^+ \varphi_0(t) \leq 0$, which can be written as follows:

$$D_\tau^+ \varphi_0(t) = u_1(\tau_+)(p_1(\tau) - (1 - x_1(\tau))) = L(p_1(\tau) - (1 - x_1(\tau))) \leq 0, \quad (2.80)$$

¹ $D_\tau^+ \varphi(t) := \limsup_{h \rightarrow 0^+} (\varphi(\tau + h) - \varphi(\tau))/h$.

CHAPTER 2. PERIODIC FLOW OF RIBOSOMES

Recall that $\dot{x}_1 = u_0 - (u_0 + u_1)x_1$, $\dot{p} = (u_0 + u_1)p - u_1$. Following on $t \in (\tau, \tau + \varepsilon_1)$:

$$x(t) = \left(x(\tau) - \frac{\ell}{\ell + L}\right) e^{-(\ell+L)(t-\tau)} + \frac{\ell}{\ell + L} < \left(x(\tau) - \frac{\ell}{\ell + L}\right) e^{(\ell+L)(t-\tau)} + \frac{\ell}{\ell + L} \quad (2.81a)$$

$$p(t) = \left(p(\tau) - \frac{L}{\ell + L}\right) e^{(\ell+L)(t-\tau)} + \frac{L}{\ell + L}, \quad (2.81b)$$

where the inequality (2.81a) follows since $x(t) > \frac{\ell}{\ell+L}$ by Lemma 9.

Considiering the derivative of the switching function on $(\tau, \tau + \varepsilon_1)$ and use inequalities (2.81a), (2.80) as follows:

$$\dot{\varphi}_0(t) = L(p_1(t) + x_1(t) - 1) < L(x(\tau) + p(\tau) - 1)e^{(\ell+L)(t-\tau)} \leq 0. \quad (2.82)$$

Hence, $\dot{\varphi}_0(t) < 0$ on $(\tau, \tau + \varepsilon_1)$. From $\varphi_0(\tau) = 0$, and integrating

$$\varphi_0(t) < 0 \text{ for } t \in (\tau, \tau + \varepsilon_1). \quad (2.83)$$

The claim is that this implies that $u_0(t) = \ell$ for $t \in (\tau, T]$. The proof is: For the sake of contradiction assume that $u_0(\tau + \varepsilon_1) = L$. By Lemma 10, this is only optimal if $\varphi_0(\tau + \varepsilon_1) > 0$ which contradicts (2.83) since φ_0 is continuous. Hence $(+, s_1) \rightarrow (-, +) \rightarrow (+, s_2)$ is not admissible for any $s_1, s_2 \in \mathcal{S}$. Similarly, $(+, s_1) \rightarrow (-, +) \rightarrow (0, s_2)$ is not possible since it violates continuity of φ_0 . Hence $(+, s) \rightarrow (-, +)$ is equivalent to $(+, s) \rightarrow (\square, +)$.

Similar arguments can be repeated for the other cases. \square

There are other transitions should be excluded. They are stated in the following two lemmas:

Lemma 15. *Let \mathcal{X} be an optimal trajectory. Consider two consecutive arcs. The following transition is not admissible: $(+, 0) \rightarrow (-, s)$, for any $s \in \mathcal{S}$. Similarly, $(+, 0) \rightarrow (0, s)$, $(-, 0) \rightarrow (+, s)$, $(-, 0) \rightarrow (0, s)$, $(0, +) \rightarrow (s, -)$, $(0, +) \rightarrow (s, 0)$, $(0, -) \rightarrow (s, +)$, $(0, -) \rightarrow (s, 0)$ for any $s \in \mathcal{S}$. Also, all their reverses.*

Proof. W.l.o.g, let's have the transition $(0, +) \rightarrow (+, 0)$. Let τ be the transition time. There exists $\varepsilon > 0$ such that $\varphi_1(t) \equiv 0$ for $t \in (t, t + \varepsilon)$, and (by Lemma 12) $\varphi_1(t) \equiv \bar{\varphi}_1 > 0$ for $t \in (\tau - \varepsilon, \tau)$. This implies that $\varphi_1(t)$ is discontinuous at τ ; a contradiction. The same argument can be used for the other cases. \square

CHAPTER 2. PERIODIC FLOW OF RIBOSOMES

Lemma 16. *Let \mathcal{X} be an optimal trajectory, and consider three consecutive arcs. Then, the following transition is inadmissible: $(+, 0) \rightarrow (+, +) \rightarrow (+, 0)$. Similarly, the following transitions are inadmissible $(0, +) \rightarrow (+, +) \rightarrow (0, +)$, $(-, 0) \rightarrow (-, -) \rightarrow (-, 0)$, $(0, -) \rightarrow (-, -) \rightarrow (0, -)$*

Proof. Let the arcs be defined on the following time intervals $(\tau_1 - \varepsilon_1, \tau_1)$, (τ_1, τ_2) , $(\tau_2, \tau_2 + \varepsilon_2)$ for some $\tau_1, \tau_2, \varepsilon_1, \varepsilon_2 > 0$. Then on the first arc, Lemma 11 gives that $x_1(t) \equiv c_0$ for $t \in (\tau_1 - \varepsilon_1, \tau_1)$. On the second arc, the system is represented by $\dot{x}_1 = L(1 - 2x)$, with $x(\tau_1) = c_0$, and the third arc we have $x(\tau_2) \equiv c_0$ for $t \in (\tau_2, \tau_2 + \varepsilon)$. If $c_0 \neq \frac{1}{2}$, then it follows x_1 is discontinuous at τ_2 ; a contradiction. If $c_0 = \frac{1}{2}$, then this implies that $x_1(t) \equiv c_0$ on the second arc which implies that $\varphi_0(t) \equiv 0$ on that arc, i.e it has a sign $(0, +)$; a contradiction. The proof is similar for the remaining cases. \square

Using Lemma 12, If an optimal trajectory has an arc with the sign $(0, 0)$, then it can not have arcs with signs $(\pm, 0)$ or $(0, \pm)$. Using the above lemmas, there is no cycle possible amongst the arc signs. So,

Proposition 17. *Let \mathcal{X} be an optimal trajectory. Then, it can not have more than 9 arcs.*

The proof consists of starting from an arc sign, and then tracing the longest possible arc transitions. All such paths will terminate, and the longest one can be found. For instance, if the optimal trajectory \mathcal{X} has an arc with sign $(0, 0)$, then the transition diagram is simple. If the trajectory starts from $(+, -)$ then the longest paths are as follows:

$$(+, -) \rightarrow (0, 0) \begin{cases} \rightarrow (\boxplus, \boxminus) \\ \rightarrow (\boxminus, \boxplus) \end{cases}$$

A similar diagram can be given if the trajectory starts from $(-, +)$. If it starts from $(+, +)$ or $(-, -)$ then $(0, 0)$ cannot appear, and the diagram will be a subset of the diagram in the second case that follows.

The second case is when singular arcs can be present but without an arc with the sign $(0, 0)$. The longest path diagram is as follows:

$$(+, -) \rightarrow (+, +) \rightarrow (+, 0) \rightarrow (+, +) \begin{cases} \rightarrow (\boxminus, +) \rightarrow (\boxminus, -) \rightarrow (\boxminus, \boxplus) \\ \rightarrow (+, \boxminus) \rightarrow (-, \boxminus) \rightarrow (0, \boxminus) \rightarrow (-, \boxminus) \rightarrow (\boxplus, \boxminus) \end{cases}$$

CHAPTER 2. PERIODIC FLOW OF RIBOSOMES

All other transitions that share the first two arcs are subsets of these longer transitions above. For instance, if the trajectory starts from any of the first three arcs to get a diagram, or it can eliminate the singular arcs from the diagram above to get admissible trajectories consisting entirely of regular arcs. Also, the second arc's sign can be changed to $(-, -)$ and a dual diagram can be given. Similar transition diagrams can be given when we start with $(-, +)$ instead.

2.4.5 Suboptimality of admissible switching patterns

In this part, longest path, given in the previous sections, are shown to be suboptimal. The following tricks helps to reduce the number of cases that were provided in Prop. 17.

Lemma 18. *Any trajectory with n arcs that is starting and ending with the same arc can be written with $n - 1$ arcs without loss of generality.*

Proof. Consider a trajectory that starts with (s_1, s_2) arc $t \in (0, \tau_1)$ and finishes with (s_1, s_2) arc $t \in (T - \tau_2, T)$. By defining the period between for $t \in (\tau_1, T + \tau_1)$. The trajectory starts with the 2nd arc at time τ_1 and finishes at time $T + \tau_1$, where the last arc's time length is $\tau_1 + \tau_2$. \square

The following lemma, helps to derive one integral for the four optimal trajectories that were defined in Prop. 17 and include an arc with sign $(0, 0)$.

Lemma 19. *If the optimal trajectory \mathcal{X} has an arc with sign $(0, 0)$, then it can be written in the form of $(+, -) \rightarrow (0, 0) \rightarrow (-, +)$.*

Proof. From the Prop. 17 and Lemma 18, the optimal trajectory \mathcal{X} that has an arc with sign $(0, 0)$ can be written in the form of $(0, 0) \rightarrow (-, +)$, $(0, 0) \rightarrow (+, -)$, $(+, -) \rightarrow (0, 0) \rightarrow (-, +)$, and $(-, +) \rightarrow (0, 0) \rightarrow (+, -)$. The $(0, 0) \rightarrow (-, +)$, and $(-, +) \rightarrow (0, 0) \rightarrow (+, -)$ trajectories contradict the periodicity of the optimal trajectory, while $(+, -) \rightarrow (0, 0) \rightarrow (-, +)$ is equivalent to $(-, +) \rightarrow (0, 0) \rightarrow (+, -)$ by shifting the period to the starting time of the last arc of each trajectory. \square

Now, the cost function of Problem 3 can be driven, for the optimal trajectory that was defined in lemma 19. Consider that the $(+, -)$ arc switches to $(0, 0)$ trajectory at τ_1 , then switches

CHAPTER 2. PERIODIC FLOW OF RIBOSOMES

to $(-, +)$ at time $T - \tau_2$. The cost function would be:

$$J := \frac{1}{T} \int_0^T u_1(t)x_1(t)dt, \quad (2.84a)$$

$$= \frac{1}{\tau_1} \int_0^{\tau_1} u_1(t)x_1(t)dt + \frac{1}{T - \tau_1 - \tau_2} \int_{\tau_1}^{T-\tau_2} u_1(t)x_1(t)dt + \frac{1}{\tau_2} \int_{T-\tau_2}^T u_1(t)x_1(t)dt, \quad (2.84b)$$

$$= c_0\mu(E^0) + c_+\mu(E^+) + c_-\mu(E^-) + (c_+ - c_-)(b_+ - b_-) \sum_{i=1}^n \frac{t_i^+ t_i^-}{b_+ t_i^+ + b_- t_i^-}. \quad (2.84c)$$

Considering the (10) values for $-$ and $+$ signs of the arc, and c_0, c_1 for the singular value sign 0. The boundary conditions (2.65) imply that:

$$\bar{u}_0 = \frac{L\tau_1 + c_0(T - \tau_1 - \tau_2) + l\tau_2}{T}, \quad (2.85a)$$

$$\bar{u}_1 = \frac{l\tau_1 + c_1(T - \tau_1 - \tau_2) + L\tau_2}{T}. \quad (2.85b)$$

2.5 Conclusion

If so, then may be we can call this the “casino effect” the gains are never enough to compensate for the losses. This means that entertainment to a (non-trivial) periodic signal always incurs a cost, as the production rate would have been better for constant signals.

An interesting research direction is to prove that for certain general classes of contractive systems the periodic gain is one. This may be done for example by considering cases where the PMP is not only a necessary condition for optimality, but also a sufficient condition.

An interesting goal is to derive a simple to test ad-hoc procedure for determining whether the periodic gain is larger or smaller than one. A simple idea in this direction is for the case of a single periodic rate, say $\lambda(t)$. Suppose that for a constant rate $\lambda(t) \equiv a$ the steady-state output is $f(a)$. Suppose also that $f \in C^2$, and that $f'(a) > 0$. For $\varepsilon > 0$ sufficiently small, then

$$f(a + \varepsilon) - f(a) \approx \varepsilon f'(a) + \frac{\varepsilon^2}{2} f''(a) > 0, \quad (2.86)$$

i.e. when increasing a to $a + \varepsilon$ we increase the steady state-state by $\varepsilon f'(a) + \frac{\varepsilon}{2} f''(a)$. Similarly,

$$f(a - \varepsilon) - f(a) \approx -\varepsilon f'(a) + \frac{\varepsilon^2}{2} f''(a) < 0, \quad (2.87)$$

i.e. when decreasing a to $a - \varepsilon$, to reduce the steady state-state by $\varepsilon f'(a) - \frac{\varepsilon^2}{2} f''(a)$. The “total gain” when a is varied in the range $[a - \varepsilon, a + \varepsilon]$ is thus $\varepsilon^2 f''(a)$. The same result is obtained

CHAPTER 2. PERIODIC FLOW OF RIBOSOMES

when $f'(a) < 0$. This suggests that if $f''(a) > 0$ ($f''(a) < 0$) then the “total gain” is positive [negative] and it may be expected the periodic gain (for rates that vary around an average a) to be larger [smaller] than one.

To demonstrate this, note that for the RFM with $n = 1$ and $\lambda = 1$, the steady-state production rate $R = f(\lambda_0)$ with

$$f(\lambda_0) := \frac{\lambda_0}{1 + \lambda_0}, \quad (2.88)$$

so

$$f''(\lambda_0) = \frac{-2}{(1 + \lambda_0)^3} < 0, \quad (2.89)$$

and this agrees with the fact that the periodic gain is smaller than one.

On the other-hand, for the system in Example ??, for $u(t) \equiv a$, with $a > 0$, the output is $f(a) := 1/a$, so

$$f''(a) = 2a^{-3} > 0, \quad (2.90)$$

and this agrees with the fact that the periodic gain is larger than one.

Chapter 3

Bispecific T-cell engagers

Bispecific T cell engagers have proven to be a potent antibody design in cancer immunology by forming a trinary complex when binding to an immune cell and a cancer cell simultaneously. This type of antibody substitutes the role of antigen presenting cells to activate the immune cells against the cancer cells. T cell engagers should be carefully designed to have maximum potency, the immune cell-antibody-cancer cell trinary complex concentration, against tumor cells and circumvent cytokine storm in the body. A relatively high concentration of the antibody, increases the risk of cytokine storm, saturates the number of immune cell-antibody and antibody-cancer cell dimers, and hinders a potent response. A low concentration of the antibody is not sufficient to produce a potent concentration of trinary complex to activate the immune system against the cancer cells. The purpose of this study is to quantitatively investigate how the concentration of trinary complex, and distribution are dependent on the design characteristics of the bispecific antibodies, like the binding kinetics to the target receptors on the immune cells and the cancer cells. Several antibodies that are either clinically approved, or currently under clinical/preclinical development process are simulated to explore if the kinetics can be enhanced with a different design. Moreover, the identifiability analysis done in this work proves the sufficiency of steady state data for identifiability of the dissociation rates.

3.1 Introduction

BiTE has shown an strong cancer immunotherapy strategy in recent years [40–43]. BiTE technology has been proposed for treating acute myeloid leukemia [44], multiple myeloma [45], lymphoblastic leukemia [46], refractory solid tumors [47], and as a platform for targeted therapy

CHAPTER 3. BISPECIFIC T-CELL ENGAGERS

across different tumor types [48]. A list of BiTE molecules that were considered in this study is presented in table 3.1. This list is made by selecting the BiTE molecules that their binding kinetics to the targets were specified in the literature. More detailed review of the existing BiTEs or bispecific antibodies has been recently done recently by [43, 49, 50].

The targeted receptor protein of cancer cells are biomarkers of the cancer cells that have minimal expression in normal cells to have minimum off target effects. Also, BiTEs might have different chemical structure formats with different number of binding sites. The targeted receptor protein of immune cell is CD3 receptor of T cells for all the BiTEs considered in this study.

A three-body model [51] is what all bispecific antibodies have in common. In the three-body model a bispecific antibody, binding species, connects to two different target molecules, terminal species, to form a trinary complex. After the formation of dimers of the first target and the antibody, the binding kinetics can be changed based on Cooperativity factor to increase/decrease the binding affinity of the antibody molecule of the formed dimer to the second target. A positive Cooperativity factor increases the binding affinity, and it can be interpreted as the avidity factor explained in the bispecific antibody literature [52–55], where the bispecific antibody is targeting two different receptors of the same cell type for an increased specificity. The Cooperativity factor can be neglected in models of bispecific antibodies that are targeting two different cell types like BiTE, as the dimers are free in the spatial coordinates to bind to the second target. In this study, the first objective is to evaluate the design characteristics of BiTEs based on the simple model presented in figure 3.1. The BiTE antibody, X , is targeting receptors on the immune cells, T_1 which usually is the CD3 receptor of T cells, and the protein receptor of cancer cells, T_2 .

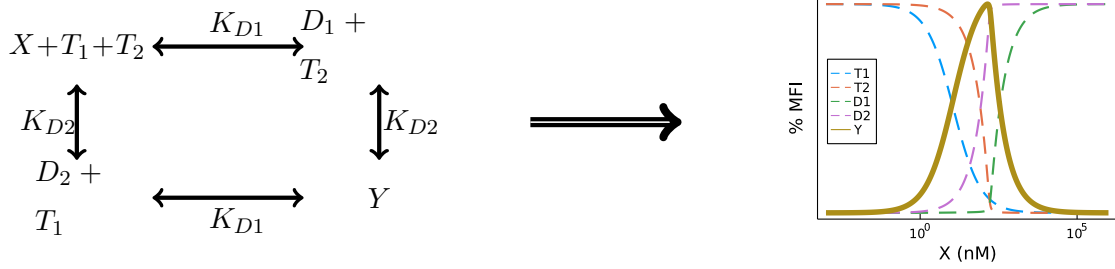


Figure 3.1: On the left side, the three-body model of BiTE, X , T_1 and T_2 are the two target receptors on immune and cancer cells, D_1 and D_2 are the dimers of bispecific antibody-immune cell and bispecific antibody-cancer cell, Y is the trimer complex, and k_{D1} and k_{D2} are the dissociation constants of the antibody binding equilibrium. The chemical reactions are visualized in a simple form to provide an intuitive idea of the reactions, specifically T_2 (T_1) is not involved in dimerization reaction between X and T_1 (T_2), i.e. the differential equations presented in (3.1) do not follow mass-action kinetics from the visualized chemical reaction network. On the right side, a nominal bell-shape pattern of the trinary complex Y in fluorescent intensity is visualized as a function of BiTE concentration. Binding kinetics and initial conditions are adopted from [56].

Table 3.1: CD3 BiTEs (sorted by the year of the referenced publication)

CD3 BiTE	Target	k_{D1} (nM)	k_{D2} (nM)	Type	Format	kDa	Ref
Blinatumomab	CD19	~ 100	~ 1	Liquid	BiTE	54	[57]
Solitomab	Ep-CAM	16 ± 12	77 ± 39	Liquid	BiTE	55	[58]
BAY2010112	PSMA	9.4 ± 4.3	47.0 ± 8.1	Solid	BiTE	55	[59]
PF-06671008	Pcad	11.5 ± 0.9	0.521 ± 0.162	Solid	DART	57	[60]
CD3 _{ϵ} L/HER2	HER2	50	0.5	Solid	KIH	> 100	[61]
CD3 _{ϵ} H/HER2	HER2	0.5	0.5	Solid	KIH	> 100	[61]
CD3 _{ϵ} VH/HER2	HER2	0.05	0.5	Solid	KIH	> 100	[61]
7370	FLT3	27	49×10^{-3}	Liquid	IgG-based	146	[62]
PF-07062119	GUCY2C	7.47 ± 0.15	23.97 ± 0.97	Solid	IgG1-FcyR	> 100	[63]
Tarlatamab	DLL3	0.64 ± 0.05	14.9 ± 0.4	Solid	HLE-BiTE	> 100	[64]
Acatatamab	PSMA	22.4 ± 2.8	14.8 ± 2	Solid	HLE-BiTE	> 100	[65]
Anti-CD79b/CD3	CD79b	12.8	1	Liquid	KIH	150	[66]

CHAPTER 3. BISPECIFIC T-CELL ENGAGERS

In the recent investigations such as [51, 56] it has been emphasised that the efficacy of BiTE, trimer concentration at the cite of action, is a bell-shape function. A relatively low or high concentration of a BiTE is not effective to produce enough number of trimer complexes to activate the immune cells against the cancer cells. At a low concentration the BiTE concentration is simply not enough to produce a potent concentration of trimer complex Y . At a high concentration the BiTE saturates the target receptor proteins on the immune cells and cancer cells, in a way that the dimers of immune cell - BiTE, D_1 , and BiTE - cancer cell, D_2 , increase and limit the number of free targets to form the trinary complex Y . Besides that, a high concentration of the BiTE can potentially cause off target side effects in the body or end up in a cytokine storm of the immune system.

In order to reproduce the bell-shape pattern of the efficacy of the BiTE to their initial concentration, four critical parameters are necessary: 1) initial concentration of target 1 T_1 , 2) initial concentration of T_2 , 3) binding kinetics/dissociation constant of the BiTE to target 1 K_{D1} , and 4) dissociation constant K_{D2} . The initial concentration of T_1 is dependent on the number of T cells in the body. Most of the BiTEs are targeting CD3 as T_1 (see table 3.1), therefore the variability of this target is based on patient to patient immune system variability. The initial concentration of T_2 is dependent on the tumor. As reported by the references presented in table 3.1, the initial concentration of tumor specific targets are generally considered to be less than $5 \times 10^3/\text{cell}$, and might be significantly different because of the fundamental difference across different cancer types. The main discussion of this study is based on the binding kinetics of the bispecific molecules.

The binding affinity of the BiTE to T_1 (CD3 on the T cells) can be significantly smaller, comparable, or significantly larger than the binding affinity to T_2 (targeted receptor protein on the cancer cells). For example, the binding affinity of Blinatumomab [57], PF-06671008 [60], and (7370) [62] to target receptor on the immune cells is great than its binding affinity to target receptor on the cancer cells. The binding affinities of Acapatamab [65], Solitomab [58], and PF-07062119 [63] to its targets is in a comparable range. On the other hand, BiTEs like BAY2010112 [59], Taralatamab [64], and REGN5458 [67] present a larger affinity to the cancer cell targets in comparison to the immune cell targets.

The binding kinetics of the BiTE molecules to each of the targets may also effect the distribution of this type of antibody at different tissues. The bio-distribution of CD3/HER2 T-cell-Dependent Bispecific (TDB), or BiTE, has been measured for different range of affinities to CD3 for the solid tumors in mouse models [61]. Recent discoveries suggest higher affinities to CD3 (lower dissociation rate k_{D1}) increases the uptake in T cell tissues, e.g. Lymph nodes, and decreases the uptake at the cite of action, e.g. Tumor Micro-Environment (TME). Therefore, lower affinities of

CHAPTER 3. BISPECIFIC T-CELL ENGAGERS

BiTE antibody molecules to CD3 is favorable in treatments designed for solid tumors.

In addition to the BiTE molecules represented in Table 3.1, other molecules are presented in literature in details. PF-06863135 [68] (150 kDa), and AMG420 [45] (54 kDa) are both designed to target BCMA for patients diagnosed with multiple myeloma. Both of the molecules have similar dissociation rate to CD3, but different dissociation rate to BCMA, 0.1 and 0.04 nM respectively. The role of binding kinetics to BCMA is discussed as an important factor in the distribution of the molecule toward different tissues in [45]. Also, the authors of [69] discussed the design and bio-distribution of AMG211 (55 kDa), a CD3/CEA BiTE molecule for patients with advanced gastrointestinal adenocarcinomas. AMG211 has a significantly high dissociation rate to CD3 310 nM in comparison with its dissociation rate toward CEA 5.5 nM. The bio-distributions of these molecules are compared computationally by [70] based on two pore pore theory. The number of BiTE molecules in this manuscript are kept limited for the simplicity of the study, and presented figures.

In the following sections a minimal mathematical model is presented with quantitative analysis of the BiTE molecules that were publicly available in the literature. Although each of the molecules presented are designed for a different target receptor of cancer cell, the targets are assumed to be equally expressed on the cancer cell surface to have a quantitative measure of their differences. At the end, a full quantitative systems pharmacology model of a nominal BiTE is given for a broader discussion on other parameters that might significantly change the optimal dosing regimen of BiTE molecules.

3.2 Three-body model and the importance of binding kinetics

Three-body model can be considered as a minimal model for the BiTE antibodies. The physiological model simulates the instant number of produced trinary complex and the occupancy of the targeted receptors immediately after exposing the culture of immune cells and cancer cells to the BiTE antibody. The degradation of the targets and antibody is neglected in this section. This is a reasonable assumption where the dissociation equilibrium is estimated to happen much faster than the receptor shedding and antibody degradation processes.

The presented model in Figure 3.1 includes six state variables to model the concentration of the BiTE antibody $X(t)$, the target receptor on the surface of the immune cells $T_1(t)$, the target receptor on the surface of the cancer cells $T_2(t)$, the dimer complex of immune cell-antibody $D_1(t)$, the dimer complex of antibody-immune cell $D_2(t)$, and the trinary complex of immune cell-antibody-

CHAPTER 3. BISPECIFIC T-CELL ENGAGERS

cancer cell $Y(t)$. The initial concentration of the dimer and trimer complexes are assumed to be zero at the starting point $D_1(0) = D_2(0) = Y(0) = 0$. The initial concentration of BiTE antibody $X(t = 0)$ is the dose concentration that is being discussed in this section. The dynamic formulation of the three-body problem for BiTE antibodies can be written the following form.

$$\dot{X} = -k_{n1}T_1X - k_{n2}T_2X + k_{f1}D_1 + k_{f2}D_2, \quad (3.1a)$$

$$\dot{T}_1 = -k_{n1}T_1X + k_{f1}D_1 - k_{n1}T_1D_2 + k_{f1}Y, \quad (3.1b)$$

$$\dot{T}_2 = -k_{n2}T_2X + k_{f2}D_2 - k_{n2}T_2D_1 + k_{f2}Y, \quad (3.1c)$$

$$\dot{D}_1 = k_{n1}T_1X - k_{f1}D_1 - k_{n2}T_2D_1 + k_{f2}Y, \quad (3.1d)$$

$$\dot{D}_2 = k_{n2}T_2X - k_{f2}D_2 - k_{n1}T_1D_2 + k_{f1}Y, \quad (3.1e)$$

$$\dot{Y} = k_{n1}T_1D_2 + k_{n2}T_2D_1 - (k_{f1} + k_{f2})Y. \quad (3.1f)$$

Note, the time functionality of the state variables is dropped for writing simplicity, and the dot sign on the top of each state variable on the left side represents the time derivative. Model 3.1 contains only four parameters: k_{n1} , k_{f1} , k_{n2} , and k_{f2} . The parameters reported from the preclinical measurements, e.g. surface resonance experiment, are based on dissociation constants of the two binding sites:

$$k_{D1} = k_{f1}/k_{n1}, \quad (3.2a)$$

$$k_{D2} = k_{f2}/k_{n2}. \quad (3.2b)$$

Dissociation constant k_D is enough to estimate the final concentration of each species in a two body binding solution, and different values of (k_n, k_f) that result in the same dissociation constant result in a faster/slower reactions to reach to the equilibrium concentration.

The steady state simulation of Model (3.1) can be a used for preclinical experiments on a dish where the formed trimer concentration at a constant time, after exposure of the BiTE to the culture of cancer cells and immune cells, is measured. Figure 3.2 represents numerical simulations with the same parameters of the Maximum Fluorescence Intensity (MFI) molecule introduced in [56]. Figures 3.2a and 3.2b are the results of the same numerical simulation setup, and different range of input, initial concentration of the BiTE molecule in the medium. The vertical axis in Figures 3.2a and 3.2b is normalized MFI. The bell-shape of the trimer projection is the focus of this section which represent existence of an optimal concentration of BiTE at the cite of action, e.g. in the MFI, to produce the maximum concentration of the trimer complex. Note how different the experimental

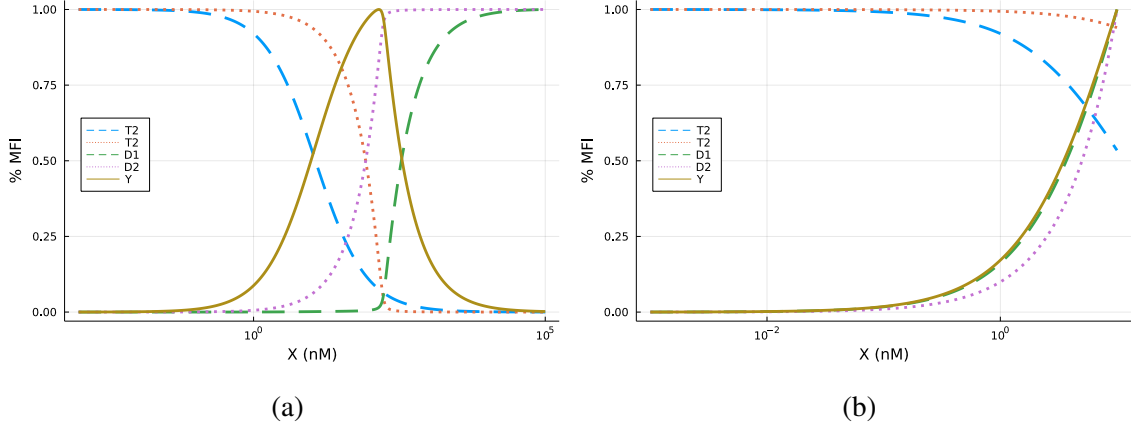


Figure 3.2: Steady state simulations of Model (3.1). The vertical axis is the normalized to the MFI levels of the variables in the experiments with different ranges of BiTE antibody initial concentration. The initial BiTE concentration range, range of horizontal axis values, in (a) is larger than (b). The plots on the left present the concentrations of the trimer and the targets, and the plots on the right side present the drug-target dimers concentrations.

results, e.g. Figure 3.2a vs Figure 3.2b, might look like when reported in MFI format with different range of MFI molecule concentration, drug dose on horizontal axis.

3.3 Identifiability

The structural identifiability analysis of model (3.1) based on a given drug $X(t)$, the first target $T1(t)$ (immune cells receptor), and the second target $T2(t)$ (protein expressed on cancer cells) data is done. Results shows that all the parameters k_{n1} , k_{f1} , k_{n2} , and k_{f2} are globally and locally identifiable. The computer software SIAN [71], structural identifiability was used to confirm this result. On the contrary, most experimental measurements are done at the steady state [57–60, 62–65].

In the remainder of the identifiability analysis performed in this section, it is proved that the dissociation rates $k_{D1} = k_{f1}/k_{n1}$, and $k_{D2} = k_{f2}/k_{n2}$ are identifiable for at most three steady state measurements. This result eliminates the need for extra measurements, e.g. surface resonance imaging, to determine the dissociation constants of BiTE molecules.

In terms of state variables Consider a steady state $X^*, T_1^*, T_2^*, D_1^*, D_2^*, Y^*$ of the system (3.1). Then the numbers $X^*, T_1^*, T_2^*, D_1^*, D_2^*, Y^*$, and $k_{n1}, k_{n2}, k_{f1}, k_{f2}$ are related by a system of

CHAPTER 3. BISPECIFIC T-CELL ENGAGERS

six polynomial equations obtained by setting the left-hand sides of (3.1) to zero. To compute the projection of its solution set to $(D_1^*, D_2^*, X^*, Y^*, k_{f1}, k_{f2})$ -coordinates (by performing elimination with Gröbner bases [72, Chapter 2, §1]) and find that the projection satisfies the following equation:

$$(D_1^* k_{f1} + D_2^* k_{f2} + X^* k_{f1} + X^* k_{f2}) (D_1^* D_2^* - X^* Y^*) = 0.$$

Since the parameters and concentrations are positive, the left bracket does not vanish, so

$$X^* = \frac{D_1^* D_2^*}{Y^*}. \quad (3.3)$$

Adding this relation to the original system of six equations and computing the projections to the $(D_1^*, D_2^*, Y^*, k_{f2}, k_{n2}, T_2^*)$ - and $(D_1^*, D_2^*, Y^*, k_{f1}, k_{n1}, T_1^*)$ -coordinates, respectively, it can be obtained that

$$(D_1^* T_2^* k_{n2} - Y^* k_{f2})(D_1^* - D_2^*) = 0, \quad \text{and} \quad (D_2^* T_1^* k_{n1} - Y^* k_{f1})(D_1^* - D_2^*) = 0.$$

For the generic case $D_1^* \neq D_2^*$,

$$T_1^* = k_{D1} \frac{Y^*}{D_2^*}, \quad \text{and} \quad T_2^* = k_{D2} \frac{Y^*}{D_1^*}. \quad (3.4)$$

In terms of first integrals The system (3.1) has three conservation laws, due to the constraints on the initial conditions: $c_1 = T_1(t) + D_1(t) + Y(t)$, $c_2 = T_2(t) + D_2(t) + Y(t)$, and $c_3 = X(t) + D_1(t) + D_2(t) + Y(t)$. Based on the initial conditions, $c_3 = X(0)$. To prove that for every positive values of c_1, c_2, c_3 , there exists at most one positive steady state, we augment the system obtained by setting the right-hand sides of (3.1) to zero with equations

$$c_1 - T_1^* - D_1^* - Y^* = c_2 - T_2^* - D_2^* - Y^* = c_3 - X^* - Y^* - D_1^* - D_2^* = 0. \quad (3.5)$$

Given the obtained system of nine equations to compute the projections (again, using Gröbner bases) of the solution set to the $(A, c_1, c_2, c_3, k_{D1}, k_{D2})$ -coordinates, where A is taken to be T_1^* or T_2^* , and find that these projections satisfy:

$$(T_1^*)^2 + (c_3 + k_{D1} - c_1)T_1^* - c_1 k_{D1} = 0 \quad \text{and} \quad (T_2^*)^2 + (c_3 + k_{D2} - c_2)T_2^* - c_2 k_{D2} = 0 \quad (3.6)$$

Consider the first equation as a quadratic equation in T_1^* . The product of the roots is equal to $-c_2 k_{D2} < 0$, so at most one of the roots is real positive, so T^* is uniquely determined. The same applies to T_1^* . Next, by computing projection to the $(D_2^*, T_1^*, T_2^*, c_1, c_2, c_3, k_{D1}, k_{D2})$ -coordinates, to find the following relation for D_2^* :

$$c_3 D_2^* + T_1^* T_2^* - c_2 T_1^* - c_1 T_2^* + c_3 T_2^* + c_1 c_2 - c_2 c_3 = 0, \quad (3.7)$$

CHAPTER 3. BISPECIFIC T-CELL ENGAGERS

which implies that D_2^* is uniquely determined. Finally, D_1^* , X^* , and Y^* are uniquely determined using the following simple consequences of (3.5):

$$D_1^* - D_2^* + T_1^* - T_2^* - c_1 + c_2 = 0, \quad Y^* + T_2^* + D_2^* - c_2 = 0, \quad \text{and} \quad X^* + D_2^* - T_1^* + c_1 - c_3 = 0. \quad (3.8)$$

Two experiments Assuming that three experiments were conducted as described above and the steady state data $(T_1^{[i]}, T_2^{[i]}, D^{[i]})$ is given for $i = 1, 2, 3$. The identification approach is to consider the first two experiments. Equations (3.3), and (3.4) are used to write the following polynomial system:

$$Y^{[i]} X^{[i]} = (c_1 - T_1^{[i]} - Y^{[i]})(c_2 - T_2^{[i]} - Y^{[i]}), \quad (3.9a)$$

$$T_1^{[i]} X^{[i]} = k_{D1}(c_1 - T_1^{[i]} - Y^{[i]}), \quad (3.9b)$$

$$T_2^{[i]} X^{[i]} = k_{D2}(c_2 - T_2^{[i]} - Y^{[i]}), \quad (3.9c)$$

$$\text{for } i = 1, 2. \quad (3.9d)$$

To compute the projection of the solution set of this system to the $(k_{D1}, k_{D2}, T_1^{[1]}, T_1^{[2]}, T_2^{[1]}, T_2^{[2]}, X^{[1]}, X^{[2]})$ -coordinates (using Gröbner bases) and find relations of the form:

$$A_1 k_{D1}^2 + A_2 k_{D1} + A_3 = 0, \quad \text{and} \quad B_1 k_{D2} + B_2 k_{D1} + B_3 = 0, \quad (3.10)$$

where $A_1, A_2, A_3, B_1, B_2, B_3$ are polynomials from $\mathbb{Q}[T_1^{[i]}, T_2^{[i]}, X^{[i]} \mid i = 1, 2]$. Furthermore, A_1 and B_1 factor as follows:

$$A_1 = X^{[1]} X^{[2]} (T_1^{[1]} X^{[2]} - T_1^{[2]} X^{[1]})(T_1^{[1]} T_2^{[1]} X^{[2]} - T_1^{[2]} T_2^{[2]} X^{[1]}), \quad (3.11a)$$

$$B_1 = T_1^{[1]} T_1^{[2]} (T_2^{[1]} X^{[2]} - T_2^{[2]} X^{[1]}). \quad (3.11b)$$

Therefore, A_1 and B_1 will not vanish as long as the ratios $\frac{X}{T_1}, \frac{X}{T_2}, \frac{X}{T_1 T_2}$ are different in the first two experiments. Equations (3.6), (3.7), and (3.8) yield formulas for the steady state in terms of $k_{D1}, k_{D2}, c_1, c_2, c_3$. These formulas are substituted in $\frac{X}{T_1}, \frac{X}{T_2}, \frac{X}{T_1 T_2}$ to obtain three non-constant functions with respect to c_3 . Therefore, outside of a set of measure zero, A_1 and B_1 will not vanish. Thus, (3.10) implies that generically, two experiments are sufficient to find k_{D1} and k_{D2} up to at most two options.

Three experiments For the three experiment case, since the projections above could be computed for the second and third experiment, not for the first and second, if $T_1^{[1]}, T_2^{[1]}, X^{[1]}$ is substituted with $T_1^{[3]}, T_2^{[3]}, X^{[3]}$ in the first equation in (3.10), there can be a true relation. This will yield one

more quadratic equation for k_{D1} , denoted by $\tilde{A}_1 k_{D1}^2 + \tilde{A}_2 k_{D1} + \tilde{A}_3 = 0$. If it is not proportional to the original equation, this will leave at most one value for k_{D1} . A sufficient condition for this non-proportionality would be $A_1 \tilde{A}_3 - \tilde{A}_1 A_3 = 0$. To check this, one can plug again the formulas of the steady state in terms of $k_{D1}, k_{D2}, c_1, c_2, c_3$ from (3.6), (3.7), and (3.8) and observe that $A_1 \tilde{A}_3 - \tilde{A}_1 A_3$ is a non-constant function in $k_{D1}, k_{D2}, c_1, c_2, c_3^{[1]}, c_3^{[2]}, c_3^{[3]}$. Therefore, $A_1 \tilde{A}_3 - \tilde{A}_1 A_3 \neq 0$ outside of a set of measure zero. Therefore, k_{D1} and k_{D2} are generically uniquely identifiable from three experiments.

3.4 Optimal binding kinetics

In this part we investigate the basic characteristics of the bell-shape response, trimer concentration presented in Figure 3.2a, to have a better understanding of the optimal binding kinetics of a BiTE antibody at the site of action, e.g. TME. The maximum concentration of the trimer complex, peak of the bell shape, and its corresponding initial BiTE antibody condition are taken as the main characteristic values of the bell-shape. The first step is to visualize the sensitivity of the peak of the bell-shape to the dissociation rates of the binding kinetics of the BiTE antibody to its targets, and target concentrations. The parameters used in this section are based on the model represented in [56] for PF-06671008 BiTE antibody for solid tumors.

Figure 3.3 represents how change of dissociation rates and initial concentration of the targets affect the peak of the trimer concentration, and its corresponding BiTE antibody concentration. From the left side of figure 3.3a, sensitivity of the maximum trimer peak to the dissociation rates, it can be observed that an increase in dissociation rates k_{D1} , and k_{D2} significantly decrease the peak of the trimer concentration. On the other hand, by looking at the right side of figure 3.3a it can be observed that the optimal concentration of BiTE (the corresponding initial concentration of BiTE antibody at the peak of the trimer concentration) will be decreased by reducing the k_{D1} only, and increased by increasing either k_{D1} or k_{D2} . This result demonstrates that higher affinity, i.e. lower value of the dissociation rates, of the BiTE antibody is not effective in changing the maximum trimer concentration at the site of action, i.g. in the TME. The sensitivity of the maximum trimer concentration, and optimal BiTE antibody initial concentration to the initial concentrations of the targets on the immune cells $T_1(0)$, and cancer cells $T_2(0)$ is visualized in one dimensional plots of Figure 3.3b. From the left side, it can be observed that the maximum trimer concentration is sensitive to $T_1(0)$ and insensitive to $T_2(0)$, which physically makes sense since the initial concentration of the first target, CD3 receptors on the immune system, is much less than the second target, P-cad protein

CHAPTER 3. BISPECIFIC T-CELL ENGAGERS

on the tumor cells, in the TME. This results is consistent with the sensitivity analysis presented by [56]. Surprisingly, any change above 0.01x, or below 100x in the initial concentration of the target $T_1(0)$ is not effective in changing optimal BiTE concentration, and significantly changes the optimal concentration BiTE antibody.

The dissociation rates k_{D1} and k_{D2} are dependent on the design of the BiTE antibody, while $T_1(0)$ and $T_2(0)$ are dependent on the tumor characteristics and variability among cancer patients. So, from the design perspective it would be ideal if the maximum trimer concentration and optimal BiTE concentration be less sensitive to the initial concentration of the targets. From the toxicity perspective, it would be favorable if a lower concentration of BiTE antibody can produce the same amount of trimer in the TME. In the one dimensional analysis presented in figure 3.3a, the optimal BiTE can be decreased as the dissociation rate of the first target k_{D1} becomes smaller, and it will result in a slightly higher trimer concentration that is favorable for efficacy.

Figure 3.4 extends the one dimensional visualizations presented in Figure 3.3 to two dimensions. The sensitivity of the maximum trimer concentration is on the left, and the sensitivity of the corresponding initial concentration of the BiTE antibody is on the right side. The red color represents a higher value of the nM concentrations in log scale, and the blue color represents lower concentrations. The vertical pattern in Figure 3.4a, and the horizontal pattern in Figure 3.4d are consistent with the conclusions made from Figure 3.3. Moreover, the contrasting colors in the top left and the bottom right of Figure 3.4b suggest that a simultaneous increase in dissociation rates k_{D1} , with a decrease in k_{D2} is favorable in reducing the required concentration of BiTE antibody to achieved the peak of the trimer concentration. A cross check between Figures 3.4a, and 3.4b indicates that the simultaneous changes in k_{D1} , and k_{D2} to reduce the required trimer concentration to achieve the maximum concentration might not be favorable in increasing the maximum trimer concentration at the TME.

3.5 Comparison between BiTE antibodies

The presented three-body model 3.1 is used here to have a quantitative measure in comparing different CD3 BiTE antibody molecules presented in Table 3.1. The antibody molecules included in this study are designed for the two general categories of solid, and liquid tumors. Although each of the molecules might be different in the distribution, metabolism, and pharmacokinetics characteristics, the three-body model is what they all have in common at the cite of action. Beside the dissociation constants k_D values presented in Table 3.1, the initial concentration of the targets is

CHAPTER 3. BISPECIFIC T-CELL ENGAGERS

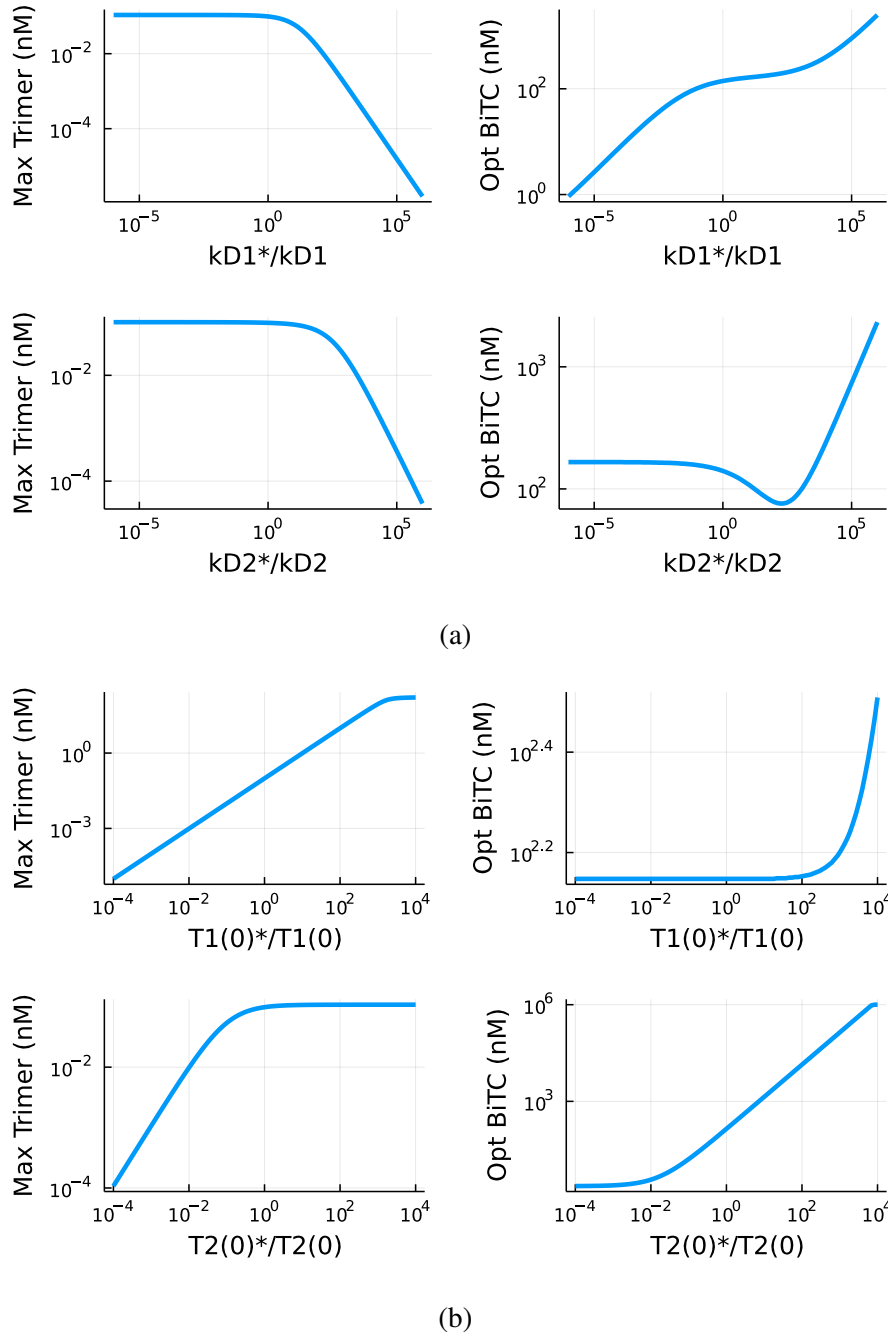


Figure 3.3: Log-log plots of bell-shape characteristics: the effects of (a) sweeping BiTE antibody dissociation rates to the targets and (b) sweeping target concentration in the TME on the optimal concentration of trimer and BiTE. The horizontal axes are log scale difference of the modified parameter (marked with a star*) and its original value. Maximum trimer concentration is the peak of the bell-shape, and Optimal BiTE is the corresponding initial antibody concentration of the peak.

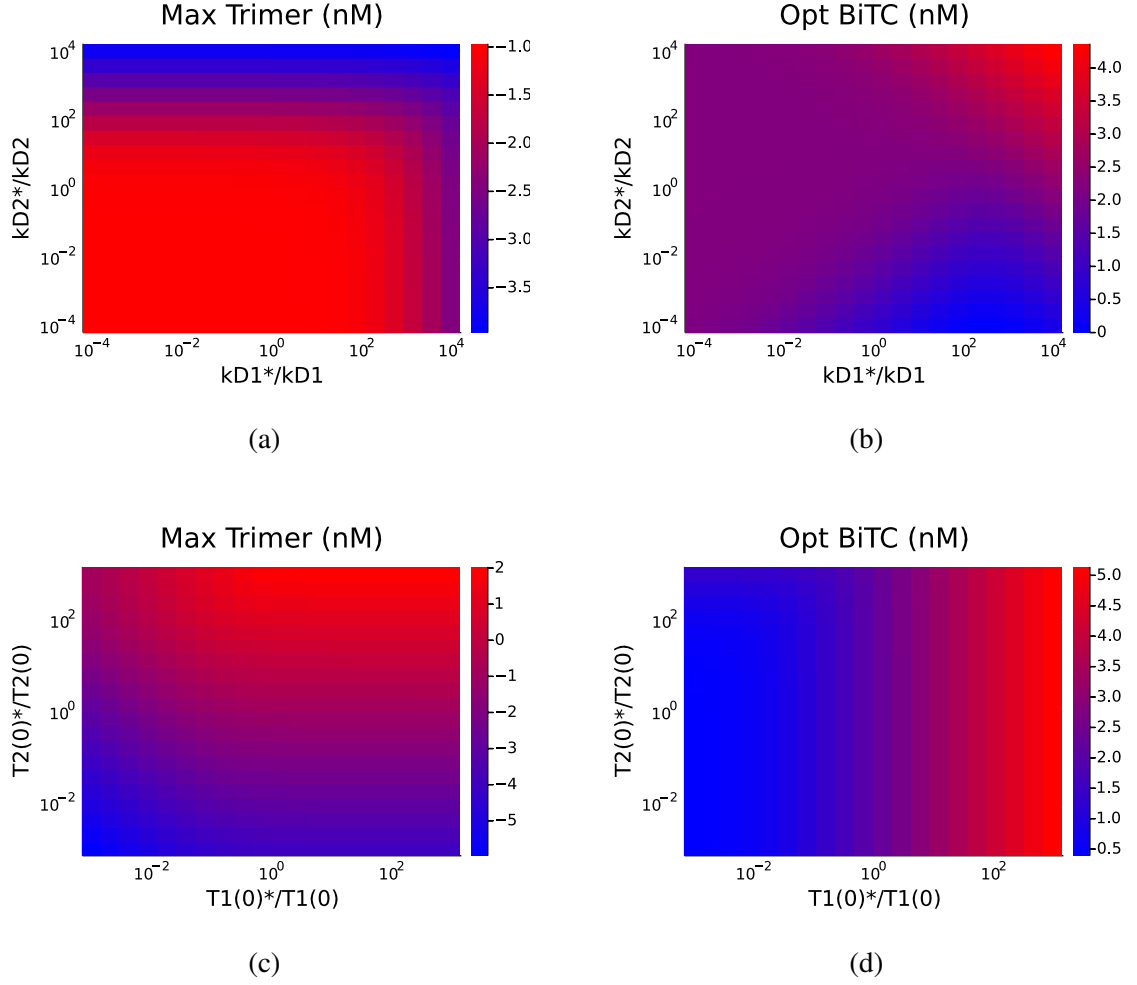


Figure 3.4: Bell-shape characteristics heatmap: the effects of sweeping the BiTE antibody dissociation rates, k_{D1} and k_{D2} , on (a) maximum of the trimer concentration of the bell-shape, and (b) corresponding, optimal, concentration of the BiTE antibody are represented on top. The effect of sweeping initial target concentrations to (c) the peak of bell-shape, and (d) optimal concentration of the antibody are presented on the bottom. The colors are plotted in log scale concentrations in nM. The horizontal and vertical axes are in log scale difference of the modified parameter (marked with a star*) and its original value.

CHAPTER 3. BISPECIFIC T-CELL ENGAGERS

necessary for computational simulations of the three-body model. As the initial concentration of the target receptors is highly dependent of the cancer type and it might vary across different regions of the tumor, the comparison between the bell-shapes of BiTE molecules should be done for different initial concentrations of the targets.

A visual comparison between the bell-shapes of the molecules considered in this study is presented in Figure 3.5. The ratio of the initial concentration of the targets ($T_1(0) : T_2(0)$) are considered to be in the range of 1:10 to 1:1000 for solid tumors (Figure 3.5a), and in the range of 10:1 to 1:10 for liquid tumors (Figure 3.5b). It can be observed that in addition to the peak of the bell-shape, and the corresponding concentration of the BiTE antibody, the width of the bell-shape varies at different ratio of the initial concentration of the targets. For instance the width of the BiTE antibody Tarlatamab increases for dense tumor, where the initial concentration of the target proteins on cancer cells is much more than the target proteins on immune cells.

An analytic formulation of the basic characteristics of the bell-shape is done by [51]. The theoretical analysis has been done to understand the sensitivity of the peak of the bell-shape to binding kinetics of the bispecific antibody to each of the targets. Moreover, the width of the bell-shape could be approximated by initial concentrations of the targets at the site of action. The presented results in this study is to have a quantitative comparisons between the BiTE molecules. For more theoretical understanding of the three-body problem, the readers are encouraged to the supplementary materials of [51].

The quantitative framework used for comparing bell-shapes of the BiTE antibody molecules at different ratios of initial concentration of the targets can be extended to continuous ratios of the targets. For this purpose, the basic characteristics of the bell-shape are extracted across different ratios between the targets, and represented in Figure 3.6. The peak of the trimer concentration is the maximum of bell-shape (on top), the corresponding BiTE concentration is the initial concentration of BiTE antibody that results in the maximum of the bell-shape (on middle), and the bell-shape width is simply the range of the BiTE antibody concentration that results in at least 50% of the maximum of the bell-shape (on bottom). For a realistic comparison between the BiTE antibodies design for solid tumors (Figure 3.6a), the left hand side of the horizontal axis should be considered, where the initial concentration of the target protein on cancer cells is much more than the initial concentration of the target protein CD3 on immune T cells. Similarly, for a realistic comparison between the BiTE antibodies designed for liquid tumors (Figure 3.6b), the right middle or right side of the horizontal axis should be taken into consideration.

From the three-body model perspective, a promising BiTE antibody is the one that creates

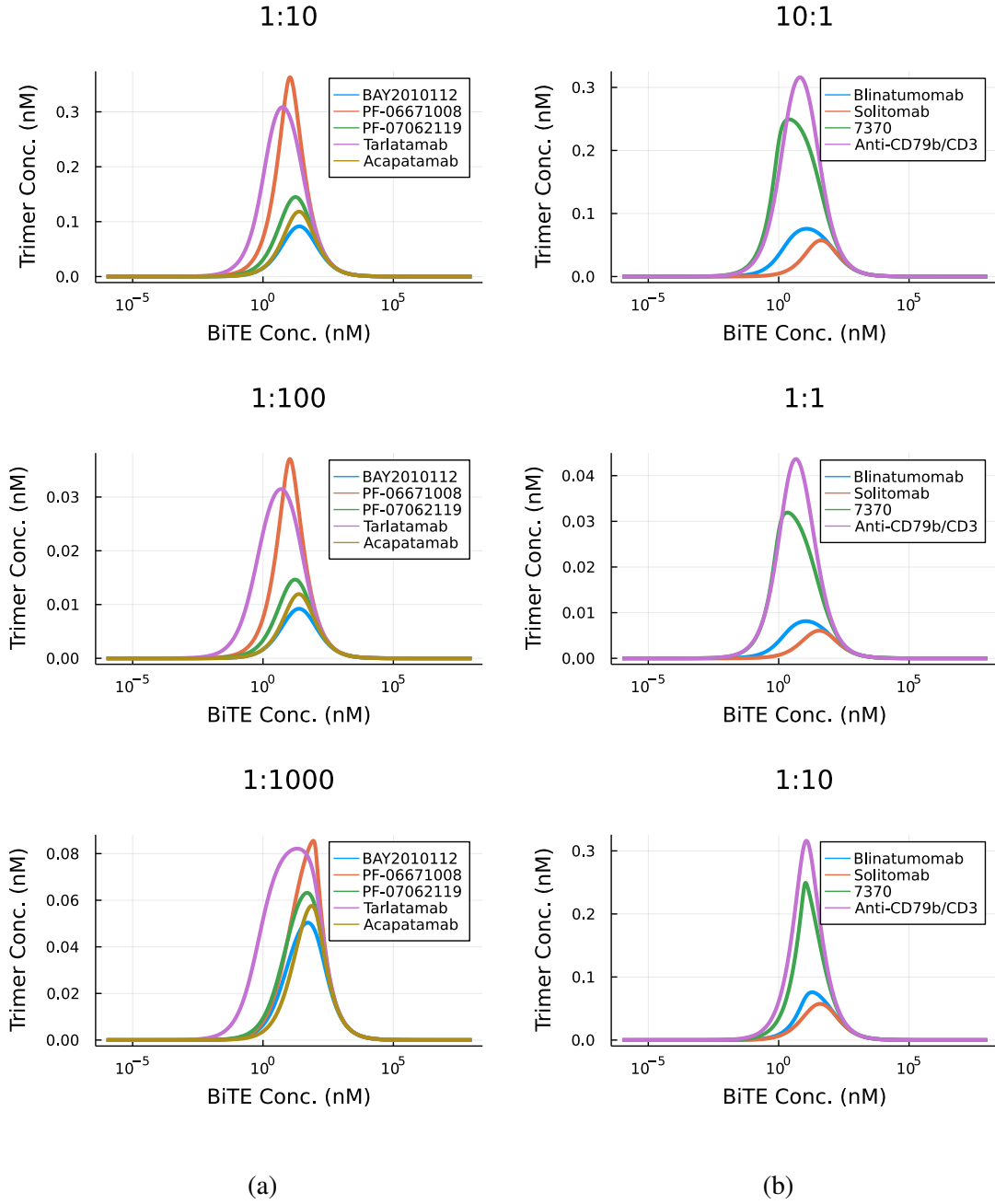


Figure 3.5: Numerical comparison between the bell shapes of BiTEs designed for (a) solid, and (b) liquid tumors. The relative concentration of the targets $T_1(0) : T_2(0)$ is printed on the top of each plot. The horizontal axes are in log scale, and the vertical axes are in linear scale.

CHAPTER 3. BISPECIFIC T-CELL ENGAGERS

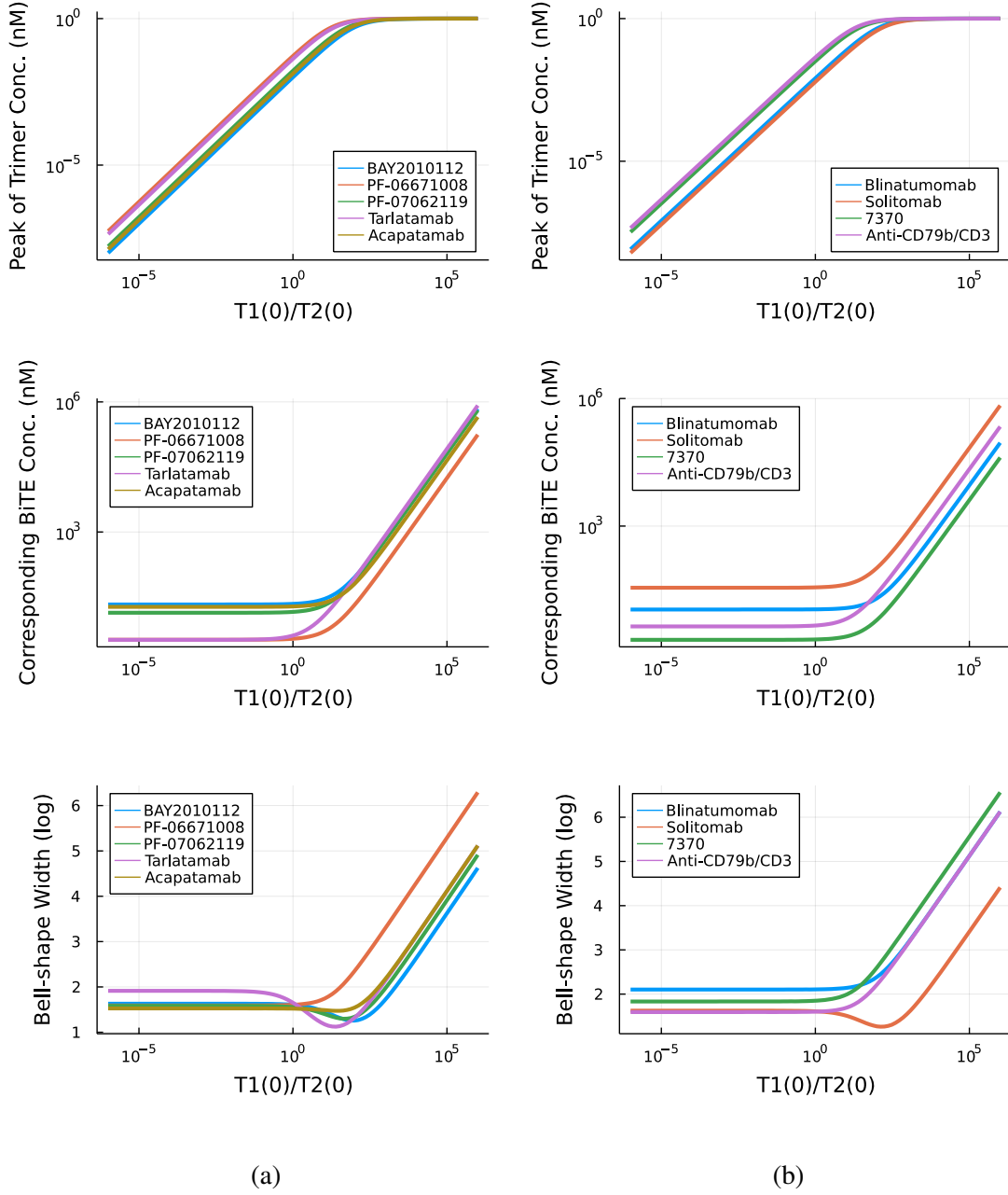


Figure 3.6: Numerical comparison between the basic characteristics of the bell-shape response of different BiTEs designed for (a) solid, and (b) liquid tumors. The top figure represent the value of the peak of bell-shape, the middle figures represent the corresponding BiTE antibody concentration at the peak of the bell-shape, and the bottom figures represent the width of the peak of the bell-shape. The relative initial concentration of the targets $T_1(0)/T_2(0)$ is visualized in log scale of the horizontal axes.

CHAPTER 3. BISPECIFIC T-CELL ENGAGERS

the most trimer concentration with the minimal initial concentration of the antibody at the cite of action. Also, to overcome natural variability among different cancers and patients it is favorable to have a BiTE antibody with minimal variation for different ratios of the initial concentrations of the targets. So, A BiTE antibody molecule is effective at the cite of action if it results in: 1) a relatively higher peak of the trimer concentration, 2) a lower corresponding concentration of the BiTE at the peak of the trimer concentration, 3) a larger width of the bell-shape. Among the molecules presented in Figure 3.6, it can be observed the BiTE molecules like 7370, and PF-06671008 are outperforming in creating a large concentration of trimer concentration of tumor with minimal initial concentration. On the other hand, BiTEantibody molecule Solitomab, is creating a stable width of the peak for a wide range of ratios between the initial concentrations of the targets. It is apparent that, stability across different initial concentration of the targets increases the consistency of the data in clinical research.

3.6 Bio-distribution

A full dynamic model for BiTE for in human for Intravenous (IV) dose is introduced in [56]. A slightly different version of this model is used here as an starting point.

CHAPTER 3. BISPECIFIC T-CELL ENGAGERS

$$\begin{aligned} \dot{X}_c = & \rho u(t) - k_{elD}X_c - k_{cp}X_c + k_{pc}X_p \frac{V_p}{V_c} - k_{cl}X_c - k_{lc}X_l \frac{V_l}{V_c} \\ & - k_{n1}X_cT1_c + k_{f1}D1_c - k_{n2}C_cT2_c + k_{f2}D2_c - k_{td}(X_c - \frac{X_t}{k_\varepsilon}) \frac{X_1 + X_2}{wV_c}, \end{aligned} \quad (3.12a)$$

$$\dot{X}_p = k_{cp}X_c \frac{V_c}{V_p} - k_{pc}X_p, \quad (3.12b)$$

$$\dot{X}_l = k_{cl}X_c \frac{V_c}{V_l} - k_{lc}X_l, \quad (3.12c)$$

$$\dot{T1}_c = -k_{ctT}T1_c + k_{tcT}T1_t \frac{M_1 + M_2}{wV_c} - k_{n1}X_cT1_c - k_{f1}D1_c, \quad (3.12d)$$

$$\dot{D1}_c = k_{n1}X_cT1_c - k_{f1}D1_c, \quad (3.12e)$$

$$\dot{T2}_c = k_{syn} - k_{deg}T2_c - k_{n2}X_cT2_c + k_{f2}D2_c, \quad (3.12f)$$

$$\dot{D2}_c = -k_{elD} * D2_c + k_{n2}X_cT2_c - k_{f2}D2_c, \quad (3.12g)$$

$$\dot{X}_t = k_{td}(X_c - \frac{X_t}{k_\varepsilon}) - k_{n1}T1_tX_t - k_{n2}T2_tX_t + k_{f1}D1_t + k_{f2}D2_t, \quad (3.12h)$$

$$\dot{T1}_t = k_{ctT}T1_c \frac{wV_c}{M_1 + M_2} - k_{tcT}T1_t - k_{n1}T1_tC_t + k_{f1}D1_t - k_{n1}T1_tD2_t + k_{f1}Y, \quad (3.12i)$$

$$\dot{T2}_t = -k_{n2}T2_tC_t + k_{f2}D2_t - k_{n2}T2_tD1_t + k_{f2}Y, \quad (3.12j)$$

$$\dot{D1}_c = k_{n1}C_cT1_c - k_{f1}D1_c \quad (3.12k)$$

$$\dot{D1}_t = k_{n1}T1_tC_t - k_{f1}D1_t - k_{n2}T2_tD1_t + k_{f2}Y, \quad (3.12l)$$

$$\dot{D2}_t = k_{n2}T2_tC_t + k_{f2}D2_t - k_{n1}T1_tD2_t + k_{f1}Y, \quad (3.12m)$$

$$\dot{Y} = k_{n1}T1_tD2_t + k_{n2}T2_tD1_t - (k_{f1} + k_{f2})Y, \quad (3.12n)$$

$$\dot{M}_1 = \frac{k_{ge}M_1(1 - \frac{M_1+M_2}{k_v})}{(1 + (\frac{k_{ge}}{k_{gl}}(M_1 + M_2))^{k_\psi})^{1/k_\psi}} - \frac{k_{max} \times Y}{kc_{50} + Y}M_1, \quad (3.12o)$$

$$\dot{M}_2 = \frac{k_{max} \times Y}{kc_{50} + Y}M_1 - M_2/k_\tau. \quad (3.12p)$$

Where X is the concentration of drug, T is the concentration of targets, D is the drug-target dimer concentration, Y is the trimer concentration, and M is the tumor volume intermediate compartment. All parameters and variables are defined in details in tables 3.2 and 3.3. The dot sign on top of the variables is a time derivative $\dot{f}(t) = \frac{df(t)}{dt}$. The differences between model 3.12 and the model presented in [56] are: 1) an extra medium for representing tissues with high concentration of immune cells, e.g. lymph nodes, 2) integrating tumor intermediate compartments into the other modules of the model, and 3) lower number of tumor intermediate compartments for representing the delay.

Table 3.2: Parameters used in model (3.12).

Value	Unit	Definition
V_c	40.2	mL/kg
V_p	211	mL/kg
V_l	92	mL/kg
k_{elD}	1.16×10^{-1}	1/h
k_{elT}	2.51	1/day
k_{cpD}	6.27×10^{-1}	1/h
k_{pcD}	1.19×10^{-1}	1/h
k_{ctT}	2×10^{-3}	1/day
k_{tcT}	5×10^{-4}	1/day
k_{n1}	1.72	1/nM/h
k_{f1}	19.66	1/h
k_{n2}	1.57	1/nM/h
k_{f2}	0.74	1/h
k_{deg}	1.5×10^{-1}	1/h
k_{syn}	$k_{deg} \times T2_c(0)$	1/h
k_{ctT}	2×10^{-3}	1/day
k_{tcT}	5×10^{-4}	1/day
k_{max}	1.32	1/day
k_{c50}	6.9×10^{-5}	nM
k_{ge}	1.9×10^{-1}	1/day
k_{gl}	1.23×10^{-1}	mL/day
k_v	6.0	mL
k_τ	3.99	day
k_ψ	20	1
w	60	kg
ρ	9.52	nM/(μ g/kg)

Table 3.3: Variables used in model (3.12).

Variable	Unit	Initial value	Definition
u	mg/kg/day	-	Input: drug dose.
X_c	nM	0.0	Antibody concentration in central compartment.
X_p	nM	0.0	Antibody concentrations in peripheral compartment.
X_t	nM	0.0	Antibody concentrations in the TME.
$T1_c$	nM	0.83	Target 1 concentration in the central compartment.
$T1_t$	nM	1.08×10^{-1}	Target 1 concentration in the TME.
$T2_c$	nM	1.1	Target 2 concentration in the central compartment.
$T2_t$	nM	1.66×10^2	Target 2 concentration in the TME.
$D1_c$	nM	0.0	Dimer drug-target 1 in the central compartment.
$D1_t$	nM	0.0	Dimer drug-target 1 in the TME.
$D2_c$	nM	0.0	Dimer drug-target 2 in the central compartment.
$D2_t$	nM	0.0	Dimer drug-target 2 in the TME.
Y	nM	0.0	Trimer concentration in the TME.
$M1$	mL	1.0	Tumor volume in growth compartment.
$M2$	mL	0.0	Tumor transduction compartment.

Computational resources

SIAN [71] is used for structural identifiability analysis, and analytical derivations. Numerical simulations and figures are produced with Julia programming language [73]. DifferentialEquations package is used numerical calculations [74]. The numerical software for reproducing the figures presented in the manuscript along with more examples is available at <https://github.com/mahdiarsadeghi/bites>.

Acknowledgment

This chapter could never be completed without the help of Irina Kareva, Gleb Pogudin, and Anup Zutshi. The discussions with Kumpal Madrasi and Abed Alnaif increased the value of this study.

Chapter 4

Epidemics

COVID-19, a highly contagious disease, has been spreading between continents and has already claimed more than 2.5 million lives globally during its first year [75], and has resulted in a worldwide economic downturn [76]. Unsurprisingly, this has sparked a renewed interest in the dynamical modeling and analysis of infectious diseases, particularly in the control theory and dynamical systems communities [77–85].

There has been much recent theoretical work revisiting, expanding, and studying dynamical and control properties of classical epidemic models so as to understand the spread of COVID-19 during quarantine and social distancing [86–91], including studies of (integral) input to state stability [92], network stability of epidemic spread [93, 94], and optimal control strategies for meta-population models [95]. These models have been used to predict the potential number of infected individuals and virus-related deaths, as well as to aid government agencies in decision making [96]. Most models are variations on the classical *SIR* model [97–99] which have been modified to more closely predict the spread of COVID-19. Some such extensions are listed below:

1. Expanding the *SIR* model to include additional population compartments. Such compartments may describe individuals that are placed under quarantine and/or in social isolation. Other models explicitly subdivide populations into both symptomatic and asymptomatic infected individuals [100–105], as it is currently thought that COVID-19 is significantly spread through *asymptomatic* individuals [106–108].
2. Modeling the effects of social distancing for an infection aware population. This can be done by changing the contact rates between the compartments, or by modeling the behavior of a

CHAPTER 4. EPIDEMICS

population that alters its social interactions because of observed infections or deaths [109, 110]. The latter technique has recently been applied to COVID-19 [111, 112].

3. Sub-dividing populations into regions, each described by *local* parameters. Such regions may be cities, neighborhoods, or communities [113]. This framework allows modelers to capture the virus spread and population mobility geographically [114–117]. These models have been recently used to understand the spread of COVID-19 in China [118], Italy [119], Netherlands and Belgium [120], and India [121, 122].

Shortening the period of time that populations are socially distanced is economically advantageous [76, 123, 124]. The main objective of this study is to reduce the disease burden (here measured as the peak of the infected population) while simultaneously minimizing the length of time that the population is socially distanced.

The starting point in modern epidemiological modeling is the Kermack-McKendrick model [97, 125] which is known as the Susceptible-Infectious-Removed (SIR) model. It assumes a well-mixed homogeneous population, and it can be written as the three-compartment model:

$$\begin{aligned}\dot{S}(t) &= -c\beta S(t)I(t), \\ \dot{I}(t) &= c\beta S(t)I(t) - \gamma I(t), \\ \dot{R}(t) &= \gamma I(t),\end{aligned}\tag{4.1}$$

where $S(t)$, $I(t)$, $R(t)$ refer to the susceptible, infective, and removed individuals at time t . The product $b = c\beta$ and the parameter γ are called the *infection rate* and the *removal rate*, respectively. We factored the infection rate as $b = c\beta$, where we call c and β the *intrinsic infection rate* and the *contact rate* respectively, to emphasize that b depends on both *biological* and *societal* conditions.

4.1 Optimal timing

Social Distancing (SD) as a form of NPI has been enacted in many countries as a form of mitigating the spread of COVID-19. There has been a large interest in mathematical modeling to aid in the prediction of both the total infected population and virus-related deaths, as well as to aid government agencies in decision making. As the virus continues to spread, there are both economic and sociological incentives to minimize time spent with strict distancing mandates enforced, and/or to adopt periodically relaxed distancing protocols, which allow for scheduled economic activity. The

CHAPTER 4. EPIDEMICS

main objective of this section is to reduce the disease burden in a population, here measured as the peak of the infected population, while simultaneously minimizing the length of time the population is socially distanced, utilizing both a single period of social distancing as well as periodic relaxation. A linear relationship is derived among the optimal start time and duration of a single interval of social distancing from an approximation of the classic epidemic *SIR* model. Furthermore, there is a sharp phase transition region in start times for a single pulse of distancing, where the peak of the infected population changes rapidly; notably, this transition occurs well *before* one would intuitively expect. By numerical investigation of more sophisticated epidemiological models designed specifically to describe the COVID-19 pandemic, we see that all share remarkably similar dynamic characteristics when contact rates are subject to periodic or one-shot changes, and hence lead us to conclude that these features are *universal* in epidemic models. On the other hand, the nonlinearity of epidemic models leads to non-monotone behavior of the peak of infected population under periodic relaxation of social distancing policies. This observation led to hypothesize that an additional single interval social distancing at a *proper time* can significantly decrease the infected peak of periodic policies, and verified numerically. While synchronous quarantine and social distancing mandates across populations effectively minimize the spread of an epidemic over the world, relaxation decisions should not be enacted at the same time for different populations.

After the shelter-in-place ordinances [126], social distancing as a form of NPI has been enacted in the United States [127], and other countries [128, 129] for reducing the spread of the virus, as neither herd immunity nor a viable vaccine yet existed [130]. Many countries have implemented strict quarantine, isolation, or social distancing policies early in the epidemic [128], while countries such as Belarus [131] and Sweden [132, 133] have taken more lenient approaches at the onset of the outbreak. Understanding optimal strategies for social distancing will both “flatten the curve” and hopefully ease the economic burden experienced due to prolonged economic stagnation [134–136]. The goal of this section is thus to investigate the response of the disease to different time-varying social distancing strategies.

4.2 Singular perturbation approach

In order to control highly-contagious and prolonged outbreaks, public health authorities intervene to institute social distancing, lock-down policies, and other NPIs. Given the high social, educational, psychological, and economic costs of NPIs, authorities tune them, alternatively tightening up or relaxing rules, with the result that, in effect, a relatively flat infection rate results.

CHAPTER 4. EPIDEMICS

For example, during the summer in parts of the United States, daily COVID-19 infection numbers dropped to a plateau. This paper approaches NPI tuning as a control-theoretic problem, starting from a simple dynamic model for social distancing based on the classical SIR epidemics model. Using a singular-perturbation approach, the plateau becomes a Quasi Steady State (QSS) of a reduced two-dimensional SIR model regulated by adaptive dynamic feedback. It is shown that the QSS can be assigned and it is globally asymptotically stable. Interestingly, the dynamic model for social distancing can be interpreted as a nonlinear integral controller. Problems of data fitting and parameter identifiability are also studied for this model. The paper also discusses how this simple model allows for a meaningful study of the effect of population size, vaccinations, and the emergence of second waves.

Bibliography

- [1] Albert Einstein and Nathan Rosen. “On gravitational waves”. In: *Journal of the Franklin Institute* 223.1 (1937), pp. 43–54.
- [2] Gregor Mendel. “Experiments in plant hybridization (1865)”. In: *Verhandlungen des naturforschenden Vereins Brünn.* Available online: www.mendelweb.org/Mendel.html (accessed on 1 January 2013) (1996).
- [3] Ronald A Fisher. “XV.—The correlation between relatives on the supposition of Mendelian inheritance.” In: *Earth and Environmental Science Transactions of the Royal Society of Edinburgh* 52.2 (1919), pp. 399–433.
- [4] B. Alberts et al. *Molecular Biology of the Cell*. 5th ed. New York: Garland Science, 2007.
- [5] Suzan Ruijtenberg et al. “Imaging Translation Dynamics of Single mRNA Molecules in Live Cells”. In: *RNA Detection*. Springer, 2018, pp. 385–404.
- [6] Marshall J Levesque and Arjun Raj. “Single-chromosome transcriptional profiling reveals chromosomal gene expression regulation”. In: *Nature Methods* 10.3 (2013), p. 246.
- [7] Jeffrey R Moffitt et al. “Molecular, spatial, and functional single-cell profiling of the hypothalamic preoptic region”. In: *Science* 362.6416 (2018), eaau5324.
- [8] James A Briggs et al. “The dynamics of gene expression in vertebrate embryogenesis at single-cell resolution”. In: *Science* 360.6392 (2018), eaar5780.
- [9] Mo Huang et al. “SAVER: gene expression recovery for single-cell RNA sequencing”. In: *Nature Methods* 15.7 (2018), p. 539.
- [10] Daniel Edsgård, Per Johnsson, and Rickard Sandberg. “Identification of spatial expression trends in single-cell gene expression data”. In: *Nature Methods* (2018).
- [11] Nicholas T Ingolia et al. “Genome-wide analysis in vivo of translation with nucleotide resolution using ribosome profiling”. In: *Science* 324.5924 (2009), pp. 218–223.

BIBLIOGRAPHY

- [12] Sina Ghaemmamghami et al. “Global analysis of protein expression in yeast”. In: *Nature* 425.6959 (2003), p. 737.
- [13] Sai Zhang et al. “ROSE: a deep learning based framework for predicting ribosome stalling”. In: *bioRxiv* (2016). URL: <https://www.biorxiv.org/content/early/2016/11/15/067108>.
- [14] Zhen Chen et al. “Evolution of sequence-defined highly functionalized nucleic acid polymers”. In: *Nature Chemistry* 10.4 (2018), p. 420.
- [15] R. K. P. Zia, J. Dong, and B. Schmittmann. “Modeling Translation in Protein Synthesis with TASEP: A Tutorial and Recent Developments”. In: *J. Statistical Physics* 144 (2011), pp. 405–428.
- [16] Tobias von der Haar. “Mathematical and Computational Modelling of Ribosomal Movement and Protein Synthesis: an overview”. In: *Computational Structural Biotechnology J.* 1 (2012), e201204002.
- [17] Yun-Bo Zhao and J. Krishnan. “mRNA translation and protein synthesis: an analysis of different modelling methodologies and a new PBN based approach”. In: *BMC Systems Biology* 8.1 (2014), p. 25.
- [18] Vidisha Singh et al. “Computational Systems Biology Approach for the Study of Rheumatoid Arthritis: From a Molecular Map to a Dynamical Model”. In: *Genomics and Computational Biology* 4.1 (2018), e100050–e100050.
- [19] Mario Andrea Marchisio. “Computational Gene Circuit Design”. In: *Introduction to Synthetic Biology*. Springer, 2018, pp. 109–129.
- [20] Shlomi Reuveni et al. “Genome-scale analysis of translation elongation with a ribosome flow model”. In: *PLoS computational biology* 7.9 (2011), e1002127.
- [21] R. A. Blythe and M. R. Evans. “Nonequilibrium steady states of matrix-product form: a solver’s guide”. In: 40.46 (2007), R333–R441.
- [22] Marc Torrent et al. “Cells alter their tRNA abundance to selectively regulate protein synthesis during stress conditions”. In: *Science Signaling* 11.546 (2018).
- [23] Alon Diamant et al. “The extent of ribosome queuing in budding yeast”. In: 14 (2018), pp. 1–21.

BIBLIOGRAPHY

- [24] S. A. Small et al. “Endosomal Traffic Jams Represent a Pathogenic Hub and Therapeutic Target in Alzheimer’s Disease”. In: *Trends Neurosci.* 40 (2017), pp. 592–602.
- [25] Michael Margaliot and Tamir Tuller. “Stability analysis of the ribosome flow model”. In: 9.5 (2012), pp. 1545–1552.
- [26] G. Poker et al. “Maximizing protein translation rate in the nonhomogeneous ribosome flow model: A convex optimization approach”. In: *J. Royal Society Interface* 11.100 (2014), p. 20140713.
- [27] R. A. Horn and C. R. Johnson. *Matrix Analysis*. 2nd ed. Cambridge University Press, 2013.
- [28] Silvia Noschese, Lionello Pasquini, and Lothar Reichel. “Tridiagonal Toeplitz matrices: properties and novel applications”. In: *Numerical Linear Algebra with Applications* 20.2 (2013), pp. 302–326.
- [29] Michael Margaliot, Eduardo D. Sontag, and Tamir Tuller. “Entrainment to periodic initiation and transition rates in a computational model for gene translation”. In: *PloS one* 9.5 (2014), e96039.
- [30] M. Margaliot, E. D. Sontag, and T. Tuller. “Contraction After Small Transients”. In: *Automatica* 67 (2016), pp. 178–184.
- [31] Michael Margaliot, Tamir Tuller, and Eduardo D. Sontag. “Checkable Conditions for Contraction After Small Transients in Time and Amplitude”. In: *Feedback Stabilization of Controlled Dynamical Systems: In Honor of Laurent Praly*. Ed. by Nicolas Petit. Cham, Switzerland: Springer International Publishing, 2017, pp. 279–305.
- [32] S. Coogan and M. Margaliot. “Approximating the Steady-State Periodic Solutions of Contractive Systems”. In: (2018).
- [33] Leon Glass and Michael C Mackey. “A simple model for phase locking of biological oscillators”. In: *Journal of Mathematical Biology* 7.4 (1979), pp. 339–352.
- [34] Zahra Aminzare and Eduardo D Sontag. “Contraction methods for nonlinear systems: A brief introduction and some open problems”. In: *53rd IEEE Conference on Decision and Control*. IEEE. 2014, pp. 3835–3847.
- [35] Winfried Lohmiller and Jean-Jacques E Slotine. “On contraction analysis for non-linear systems”. In: *Automatica* 34.6 (1998), pp. 683–696.
- [36] Lev Semenovich Pontryagin. *Mathematical Theory of Optimal Processes*. Routledge, 1962.

BIBLIOGRAPHY

- [37] Ernest Bruce Lee and Lawrence Markus. *Foundations of Optimal Control Theory*. Wiley, 1967.
- [38] Daniel Liberzon. *Calculus of Variations and Optimal Control Theory: A Concise Introduction*. Princeton University Press, 2011.
- [39] Yoram Zarai et al. “Controllability analysis and control synthesis for the ribosome flow model”. In: 15.4 (2018), pp. 1351–1364.
- [40] Julia Stieglmaier, Jonathan Benjamin, and Dirk Nagorsen. “Utilizing the BiTE (bispecific T-cell engager) platform for immunotherapy of cancer”. In: *Expert opinion on biological therapy* 15.8 (2015), pp. 1093–1099.
- [41] T Yuraszeck, S Kasichayanula, and JE Benjamin. “Translation and clinical development of bispecific T-cell engaging antibodies for cancer treatment”. In: *Clinical Pharmacology & Therapeutics* 101.5 (2017), pp. 634–645.
- [42] Alison Betts and Piet H van der Graaf. “Mechanistic quantitative pharmacology strategies for the early clinical development of bispecific antibodies in oncology”. In: *Clinical Pharmacology & Therapeutics* 108.3 (2020), pp. 528–541.
- [43] Zheng Tian et al. “Bispecific T cell engagers: an emerging therapy for management of hematologic malignancies”. In: *Journal of Hematology & Oncology* 14.1 (2021), pp. 1–18.
- [44] George S Laszlo et al. “Cellular determinants for preclinical activity of a novel CD33/CD3 bispecific T-cell engager (BiTE) antibody, AMG 330, against human AML”. In: *Blood, The Journal of the American Society of Hematology* 123.4 (2014), pp. 554–561.
- [45] S Hipp et al. “A novel BCMA/CD3 bispecific T-cell engager for the treatment of multiple myeloma induces selective lysis in vitro and in vivo”. In: *Leukemia* 31.8 (2017), pp. 1743–1751.
- [46] Max S Topp et al. “Phase II trial of the anti-CD19 bispecific T cell-engager blinatumomab shows hematologic and molecular remissions in patients with relapsed or refractory B-precursor acute lymphoblastic leukemia”. In: *Journal of Clinical Oncology* 32.36 (2014), pp. 4134–4140.
- [47] Maxim Kebenko et al. “A multicenter phase 1 study of solitomab (MT110, AMG 110), a bispecific EpCAM/CD3 T-cell engager (BiTE®) antibody construct, in patients with refractory solid tumors”. In: *Oncoimmunology* 7.8 (2018), e1450710.

BIBLIOGRAPHY

- [48] Hermann Einsele et al. “The BiTE (bispecific T-cell engager) platform: Development and future potential of a targeted immuno-oncology therapy across tumor types”. In: *Cancer* 126.14 (2020), pp. 3192–3201.
- [49] Nimish Gera. *The evolution of bispecific antibodies*. 2022.
- [50] Peter N Morcos et al. “Quantitative Clinical Pharmacology of T-Cell Engaging Bispecifics: Current Perspectives and Opportunities”. In: *Clinical and Translational Science* 14.1 (2021), pp. 75–85.
- [51] Eugene F Douglass Jr et al. “A comprehensive mathematical model for three-body binding equilibria”. In: *Journal of the American Chemical Society* 135.16 (2013), pp. 6092–6099.
- [52] John J Rhoden, Gregory L Dyas, and Victor J Wroblewski. “A modeling and experimental investigation of the effects of antigen density, binding affinity, and antigen expression ratio on bispecific antibody binding to cell surface targets”. In: *Journal of Biological Chemistry* 291.21 (2016), pp. 11337–11347.
- [53] Bram G Sengers et al. “Modeling bispecific monoclonal antibody interaction with two cell membrane targets indicates the importance of surface diffusion”. In: *MAbs*. Vol. 8. 5. Taylor & Francis. 2016, pp. 905–915.
- [54] Brian D Harms et al. “Understanding the role of cross-arm binding efficiency in the activity of monoclonal and multispecific therapeutic antibodies”. In: *Methods* 65.1 (2014), pp. 95–104.
- [55] Eric Neil Kaufman and Rakesh K Jain. “Effect of bivalent interaction upon apparent antibody affinity: experimental confirmation of theory using fluorescence photobleaching and implications for antibody binding assays”. In: *Cancer research* 52.15 (1992), pp. 4157–4167.
- [56] Alison Betts et al. “A translational quantitative systems pharmacology model for CD3 bispecific molecules: application to quantify T cell-mediated tumor cell killing by P-cadherin LP DART®”. In: *The AAPS journal* 21.4 (2019), pp. 1–16.
- [57] Torsten Dreier et al. “Extremely potent, rapid and costimulation-independent cytotoxic T-cell response against lymphoma cells catalyzed by a single-chain bispecific antibody”. In: *International journal of cancer* 100.6 (2002), pp. 690–697.
- [58] Klaus Brischwein et al. “MT110: a novel bispecific single-chain antibody construct with high efficacy in eradicating established tumors”. In: *Molecular immunology* 43.8 (2006), pp. 1129–1143.

BIBLIOGRAPHY

- [59] Matthias Friedrich et al. “Regression of human prostate cancer xenografts in mice by AMG 212/BAY2010112, a novel PSMA/CD3-Bispecific BiTE antibody cross-reactive with non-human primate antigens”. In: *Molecular cancer therapeutics* 11.12 (2012), pp. 2664–2673.
- [60] Adam R Root et al. “Development of PF-06671008, a highly potent anti-P-cadherin/anti-CD3 bispecific DART molecule with extended half-life for the treatment of cancer”. In: *Antibodies* 5.1 (2016), p. 6.
- [61] Danielle Mandikian et al. “Relative target affinities of T-cell–dependent bispecific antibodies determine biodistribution in a solid tumor mouse model”. In: *Molecular cancer therapeutics* 17.4 (2018), pp. 776–785.
- [62] Yik Andy Yeung et al. “An optimized full-length FLT3/CD3 bispecific antibody demonstrates potent anti-leukemia activity and reversible hematological toxicity”. In: *Molecular Therapy* 28.3 (2020), pp. 889–900.
- [63] Divya Mathur et al. “A Novel GUCY2C-CD3 T-Cell Engaging Bispecific Construct (PF-07062119) for the Treatment of Gastrointestinal CancersA GUCY2C-CD3 Bispecific Targets Gastrointestinal Cancers”. In: *Clinical Cancer Research* 26.9 (2020), pp. 2188–2202.
- [64] Michael J Giffin et al. “AMG 757, a half-life extended, DLL3-targeted bispecific T-cell engager, shows high potency and sensitivity in preclinical models of small-cell lung cancer”. In: *Clinical Cancer Research* 27.5 (2021), pp. 1526–1537.
- [65] Petra Deegen et al. “The PSMA-targeting half-life extended BiTE therapy AMG 160 has potent antitumor activity in preclinical models of metastatic castration-resistant prostate cancer”. In: *Clinical Cancer Research* 27.10 (2021), pp. 2928–2937.
- [66] Rajbharan Yadav et al. “Nonclinical Pharmacokinetics and Pharmacodynamics Characterization of Anti-CD79b/CD3 T Cell-Dependent Bispecific Antibody Using a Surrogate Molecule: A Potential Therapeutic Agent for B Cell Malignancies”. In: *Pharmaceutics* 14.5 (2022), p. 970.
- [67] Eric Smith et al. *Bispecific Anti-BCMA x Anti-CD3 Antibodies and Uses Thereof*. US Patent App. 16/516,028. Jan. 2020.
- [68] Siler H Panowski et al. “Preclinical efficacy and safety comparison of CD3 bispecific and ADC modalities targeting BCMA for the treatment of multiple myeloma”. In: *Molecular cancer therapeutics* 18.11 (2019), pp. 2008–2020.

BIBLIOGRAPHY

- [69] Kirsten L Moek et al. “⁸⁹Zr-labeled Bispecific T-cell Engager AMG 211 PET Shows AMG 211 Accumulation in CD3-rich Tissues and Clear, Heterogeneous Tumor Uptake⁸⁹Zr-bispecific T-cell Engager PET in Patients with Cancer”. In: *Clinical Cancer Research* 25.12 (2019), pp. 3517–3527.
- [70] Tomoki Yoneyama et al. “Leveraging a physiologically based quantitative translational modeling platform for designing bispecific T cell engagers for treatment of multiple myeloma”. In: *bioRxiv* (2021).
- [71] Hoon Hong et al. “SIAN: software for structural identifiability analysis of ODE models”. In: *Bioinformatics* 35.16 (2019), pp. 2873–2874.
- [72] David A. Cox, John Little, and Donal O’Shea. *Using Algebraic Geometry*. Springer New York, NY, 2005. URL: <https://doi.org/10.1007/b138611>.
- [73] Jeff Bezanson et al. “Julia: A fresh approach to numerical computing”. In: *SIAM Review* 59.1 (2017), pp. 65–98.
- [74] Christopher Rackauckas and Qing Nie. “DifferentialEquations.jl – A Performant and Feature-Rich Ecosystem for Solving Differential Equations in Julia”. In: *The Journal of Open Research Software* 5.1 (2017). DOI: 10.5334/jors.151.
- [75] World Health Organization et al. *WHO Coronavirus Disease (COVID-19) Dashboard*. Geneva: World Health Organization; 2020.
- [76] Olivier Coibion, Yuriy Gorodnichenko, and Michael Weber. *The Cost of the COVID-19 Crisis: Lockdowns, Macroeconomic Expectations, and Consumer Spending*. Tech. rep. National Bureau of Economic Research, 2020.
- [77] Joshua S Weitz et al. “Awareness-driven behavior changes can shift the shape of epidemics away from peaks and toward plateaus, shoulders, and oscillations”. In: *Proc. Natl. Acad. Sci. U. S. A.* 117.51 (2020), pp. 32764–32771.
- [78] Michelangelo Bin et al. “On fast multi-shot epidemic interventions for post lock-down mitigation: Implications for simple COVID-19 models”. In: *arXiv preprint arXiv:2003.09930* (2020).
- [79] Elisa Franco. “A feedback SIR (fSIR) model highlights advantages and limitations of infection-based social distancing”. In: *arXiv preprint arXiv:2004.13216* (2020).

BIBLIOGRAPHY

- [80] Dylan H Morris et al. “Optimal, near-optimal, and robust epidemic control”. In: *arXiv preprint arXiv:2004.02209* (2020).
- [81] Giulia Giordano et al. “Modelling the COVID-19 epidemic and implementation of population-wide interventions in Italy”. In: *Nature Medicine* (2020), pp. 1–6.
- [82] Yunxiu Zhou, Simon A Levin, and Naomi Ehrich Leonard. “Active Control and Sustained Oscillations in actSIS Epidemic Dynamics”. In: *3rd IFAC Workshop on Cyber-Physical & Human Systems*. 2020.
- [83] Matthew D Johnston and Bruce Pell. “A dynamical framework for modeling fear of infection and frustration with social distancing in COVID-19 spread”. In: *arXiv preprint arXiv:2008.06023* (2020).
- [84] Jana L Gevertz et al. “A novel COVID-19 epidemiological model with explicit susceptible and asymptomatic isolation compartments reveals unexpected consequences of timing social distancing”. In: *J. Theor. Biol.* 510 (2021), p. 110539.
- [85] Mahdiar Sadeghi, James Greene, and Eduardo Sontag. “Universal features of epidemic models under social distancing guidelines”. In: *bioRxiv* (2020).
- [86] Esteban A. Hernandez-Vargas and Jorge X. Velasco-Hernandez. “In-host Mathematical Modelling of COVID-19 in Humans”. In: *Annual Reviews in Control* 50 (2020), pp. 448–456. ISSN: 1367-5788. DOI: <https://doi.org/10.1016/j.arcontrol.2020.09.006>. URL: <http://www.sciencedirect.com/science/article/pii/S1367578820300638>.
- [87] Philip E. Paré, Carolyn L. Beck, and Tamer Başar. “Modeling, estimation, and analysis of epidemics over networks: An overview”. In: *Annual Reviews in Control* 50 (2020), pp. 345–360. ISSN: 1367-5788. DOI: <https://doi.org/10.1016/j.arcontrol.2020.09.003>. URL: <http://www.sciencedirect.com/science/article/pii/S1367578820300614>.
- [88] Emeric Scharbarg et al. “From the hospital scale to nationwide: observability and identification of models for the COVID-19 epidemic waves”. In: *Annual Reviews in Control* 50 (2020), pp. 409–416. ISSN: 1367-5788. DOI: <https://doi.org/10.1016/j.arcontrol.2020.09.007>. URL: <http://www.sciencedirect.com/science/article/pii/S136757882030064X>.

BIBLIOGRAPHY

- [89] Santosh Ansumali et al. “Modelling a pandemic with asymptomatic patients, impact of lockdown and herd immunity, with applications to SARS-CoV-2”. In: *Annual Reviews in Control* 50 (2020), pp. 432–447. ISSN: 1367-5788. DOI: <https://doi.org/10.1016/j.arcontrol.2020.10.003>. URL: <http://www.sciencedirect.com/science/article/pii/S1367578820300699>.
- [90] Esteban A. Hernandez-Vargas et al. “First special section on systems and control research efforts against COVID-19 and future pandemics”. In: *Annual Reviews in Control* 50 (2020), pp. 343–344. ISSN: 1367-5788. DOI: <https://doi.org/10.1016/j.arcontrol.2020.10.007>. URL: <http://www.sciencedirect.com/science/article/pii/S1367578820300730>.
- [91] Pablo Abuin et al. “Characterization of SARS-CoV-2 dynamics in the host”. In: *Annual Reviews in Control* 50 (2020), pp. 457–468. ISSN: 1367-5788. DOI: <https://doi.org/10.1016/j.arcontrol.2020.09.008>. URL: <http://www.sciencedirect.com/science/article/pii/S1367578820300651>.
- [92] Hiroshi Ito. “Feedback control on immigration to reduce spread of infectious diseases with an ISS guarantee”. In: *2020 59th Annual Conference of the Society of Instrument and Control Engineers of Japan (SICE)*. IEEE. 2020, pp. 736–741.
- [93] Canrong Tian, Qunying Zhang, and Lai Zhang. “Global stability in a networked SIR epidemic model”. In: *Applied Mathematics Letters* (2020), p. 106444.
- [94] Fangzhou Liu et al. “On the Stability of the Endemic Equilibrium of A Discrete-Time Networked Epidemic Model”. In: *arXiv preprint arXiv:2001.07451* (2020).
- [95] Yujing Liu et al. “Epidemic spreading on midscopic multi-layer network with optimal control mechanism”. In: *Physica A: Statistical Mechanics and its Applications* 537 (2020), p. 122775.
- [96] Greg Stewart, Klaskevan Heusden, and Guy A Dumont. “How control theory can help us control COVID-19”. In: *IEEE Spectrum* 57.6 (2020), pp. 22–29.
- [97] William Ogilvy Kermack and Anderson G McKendrick. “A contribution to the mathematical theory of epidemics”. In: *Proceedings of the royal society of london. Series A, Containing papers of a mathematical and physical character* 115.772 (1927), pp. 700–721.
- [98] Fred Brauer, Carlos Castillo-Chavez, and Zhilan Feng. *Mathematical Models in Epidemiology*. Springer, 2019.

BIBLIOGRAPHY

- [99] Giacomo Albi, Lorenzo Pareschi, and Mattia Zanella. “Control with uncertain data of socially structured compartmental epidemic models”. In: *arXiv preprint arXiv:2004.13067* (2020).
- [100] Jana L Gevertz et al. “A novel COVID-19 epidemiological model with explicit susceptible and asymptomatic isolation compartments reveals unexpected consequences of timing social distancing”. In: *Journal of Theoretical Biology* 510 (2020), p. 110539.
- [101] Weijie Pang. “Public health policy: COVID-19 epidemic and SEIR model with asymptomatic viral carriers”. In: *arXiv preprint arXiv:2004.06311* (2020).
- [102] Aritz Etxeberria-Iriondo, Manuel De la Sen, and Santiago Alonso-Quesada. “A New Epidemic Model Under Vaccination”. In: *2019 14th IEEE Conference on Industrial Electronics and Applications (ICIEA)*. IEEE. 2019, pp. 2388–2392.
- [103] Tingzhe Sun and Dan Weng. “Estimating the Effects of Asymptomatic and Imported Patients on COVID-19 Epidemic Using Mathematical Modeling”. In: *Journal of Medical Virology* (2020).
- [104] Giuseppe Gaeta. “Asymptomatic infectives and R_0 for COVID”. In: *arXiv preprint arXiv:2003.14098* (2020).
- [105] Amirarsalan Rajabi et al. “Investigating dynamics of COVID-19 spread and containment with agent-based modeling”. In: *medRxiv* (2020).
- [106] Yan Bai et al. “Presumed asymptomatic carrier transmission of COVID-19”. In: *Jama* 323.14 (2020), pp. 1406–1407.
- [107] Xingxia Yu and Rongrong Yang. “COVID-19 transmission through asymptomatic carriers is a challenge to containment”. In: *Influenza and Other Respiratory Viruses* (2020).
- [108] Zhiliang Hu et al. “Clinical characteristics of 24 asymptomatic infections with COVID-19 screened among close contacts in Nanjing, China”. In: *Science China Life Sciences* (2020), pp. 1–6.
- [109] KM Ariful Kabir, Kazuki Kuga, and Jun Tanimoto. “Analysis of SIR epidemic model with information spreading of awareness”. In: *Chaos, Solitons & Fractals* 119 (2019), pp. 118–125.
- [110] Timothy C Reluga. “Game theory of social distancing in response to an epidemic”. In: *PLoS computational biology* 6.5 (2010).

BIBLIOGRAPHY

- [111] Elisa Franco. “A feedback SIR (fSIR) model highlights advantages and limitations of infection-based social distancing”. In: *arXiv preprint arXiv:2004.13216* (2020).
- [112] Navid Ghaffarzadegan and Hazhir Rahmandad. “Simulation-based Estimation of the Spread of COVID-19 in Iran”. In: *medRxiv* (2020).
- [113] Bing Wang et al. “Network structure-based interventions on spatial spread of epidemics in metapopulation networks”. In: *Physical Review E* 102.6 (2020), p. 062306.
- [114] Matteo Chinazzi et al. “The effect of travel restrictions on the spread of the 2019 novel coronavirus (COVID-19) outbreak”. In: *Science* 368.6489 (2020), pp. 395–400.
- [115] Seth Flaxman et al. “Estimating the effects of non-pharmaceutical interventions on COVID-19 in Europe”. In: *Nature* (2020), pp. 1–8.
- [116] Xue-Feng San, Zhi-Cheng Wang, and Zhaosheng Feng. “Spreading speed and traveling waves for an epidemic model in a periodic patchy environment”. In: *Communications in Nonlinear Science and Numerical Simulation* (2020), p. 105387.
- [117] Atefe Darabi and Milad Siami. “Centrality in Epidemic Networks with Time-Delay: A Decision-Support Framework for Epidemic Containment”. In: *arXiv preprint arXiv:2010.00398* (2020).
- [118] Moritz UG Kraemer et al. “The effect of human mobility and control measures on the COVID-19 epidemic in China”. In: *Science* 368.6490 (2020), pp. 493–497.
- [119] Marino Gatto et al. “Spread and dynamics of the COVID-19 epidemic in Italy: Effects of emergency containment measures”. In: *Proceedings of the National Academy of Sciences* 117.19 (2020), pp. 10484–10491.
- [120] Eline van den Broek-Altenburg and Adam Atherly. “Adherence to COVID-19 Policy Measures: Behavioral Insights from the Netherlands and Belgium”. In: *Available at SSRN* 3692644 (2020).
- [121] Bhalchandra S Pujari and Snehal M Shekatkar. “Multi-city modeling of epidemics using spatial networks: Application to 2019-nCov (COVID-19) coronavirus in India”. In: *medRxiv* (2020).
- [122] Buddhananda Banerjee, Pradumn Kumar Pandey, and Bibhas Adhikari. “A model for the spread of an epidemic from local to global: A case study of COVID-19 in India”. In: *arXiv preprint arXiv:2006.06404* (2020).

BIBLIOGRAPHY

- [123] Cristina Arellano, Yan Bai, and Gabriel P Mihalache. *Deadly Debt Crises: COVID-19 in Emerging Markets*. Working Paper 27275. National Bureau of Economic Research, May 2020. DOI: 10.3386/w27275. URL: <http://www.nber.org/papers/w27275>.
- [124] Tommy Andersson et al. “Optimal Trade-Off Between Economic Activity and Health During an Epidemic”. In: *arXiv preprint arXiv:2005.07590* (2020).
- [125] Herbert W Hethcote. “The mathematics of infectious diseases”. In: *SIAM Review* 42.4 (2000), pp. 599–653.
- [126] Austin L Wright et al. “Poverty and economic dislocation reduce compliance with COVID-19 shelter-in-place protocols”. In: *University of Chicago, Becker Friedman Institute for Economics Working Paper* 2020-40 (2020).
- [127] Michael S Wolf et al. “Awareness, attitudes, and actions related to COVID-19 among adults with chronic conditions at the onset of the US outbreak: a cross-sectional survey”. In: *Annals of Internal Medicine* (2020).
- [128] Tran Phuoc Bao Thu, Pham Nguyen Hong Ngoc, Nguyen Minh Hai, et al. “Effect of the social distancing measures on the spread of COVID-19 in 10 highly infected countries”. In: *Science of the Total Environment* 742 (2020), p. 140430.
- [129] Anil Sarin and Akhil Sarin. “Coronavirus Disease (COVID-19): Spread, Awareness and Strategic Containment”. In: *Journal of Communicable Diseases (E-ISSN: 2581-351X & P-ISSN: 0019-5138)* 52.1 (2020), pp. 22–31.
- [130] Anthony McDonnell et al. *COVID-19 Vaccine Predictions: Using Mathematical Modelling and Expert Opinions to Estimate Timelines and Probabilities of Success of COVID-19 Vaccines*. 2020.
- [131] Valentina Gritsenko et al. “COVID 19 Fear, Stress, Anxiety, and Substance Use Among Russian and Belarusian University Students”. In: *International Journal of Mental Health and Addiction* (2020), p. 1.
- [132] Matz Dahlberg et al. “Effects of the COVID-19 pandemic on population mobility under mild policies: Causal evidence from Sweden”. In: *arXiv preprint arXiv:2004.09087* (2020).
- [133] Sang-Wook Cho. “Quantifying the impact of nonpharmaceutical interventions during the COVID-19 outbreak: The case of Sweden”. In: *The Econometrics Journal* 23.3 (2020), pp. 323–344.

BIBLIOGRAPHY

- [134] Yonatan Berman. “The Distributional Short-Term Impact of the COVID-19 Crisis on Wages in the United States”. In: *arXiv preprint arXiv:2005.08763* (2020).
- [135] Charles Courtemanche et al. “Strong Social Distancing Measures In The United States Reduced The COVID-19 Growth Rate: Study evaluates the impact of social distancing measures on the growth rate of confirmed COVID-19 cases across the United States.” In: *Health Affairs* (2020), pp. 10–1377.
- [136] William F Maloney and Temel Taskin. “Determinants of social distancing and economic activity during COVID-19: A global view”. In: *World Bank Policy Research Working Paper* 9242 (2020).

Appendix A

First Appendix Headline

Appendix B

Second Appendix Headline